12-2016

A Comparison of Global Climate Reanalysis and Climate of South Greenland and the North Atlantic

Jeff Auger
University of Maine, jeff.auger@maine.edu

A COMPARISON OF GLOBAL CLIMATE REANALYSES AND CLIMATE OF SOUTH GREENLAND AND THE NORTH ATLANTIC

By

Jeffrey Daniel Auger

B.S. Metropolitan State University of Denver, 2013

A THESIS

Submitted in Partial Fulfillment of the

Requirements for the Degree of

Master of Science

(in Quaternary and Climate Studies)

The Graduate School

University of Maine

December 2016

Advisory Committee:

Sean D. Birkel, Research Assistant Professor, Climate Change Institute, Advisor

Kirk A. Maasch, Professor, School of Earth and Climate Sciences, Co-Advisor

Paul A. Mayewski, Professor, School of Earth and Climate Sciences, Director of Climate Change Institute

Keah C. Schuenemann, Assistant Professor, Earth and Atmospheric Science Department, Metropolitan State University of Denver

THESIS ACCEPTANCE STATEMENT

On behalf of the Graduate Committee for Jeffrey Daniel Auger, I affirm that this manuscript is the final and accepted thesis. Signatures of all committee members are on file with the Graduate School at the University of Maine, 42 Stodder Hall, Orono, Maine.

Dr. Sean D. Birkel, Research Assistant Professor Date

LIBRARY RIGHTS STATEMENT

In presenting this thesis in partial fulfillment of the requirements for an advanced degree at the University of Maine, I agree that the Library shall make it freely available for inspection. I further agree that permission for “fair use” copying of this thesis for scholarly purposes may be granted by the Librarian. It is understood that any copying or publication of this thesis for financial gain shall not be allowed without my written permission.

Signature:

Date:

A COMPARISON OF GLOBAL CLIMATE REANALYSES AND CLIMATE OF SOUTH GREENLAND AND THE NORTH ATLANTIC

By Jeffrey Daniel Auger

Thesis Advisor: Dr. Sean D. Birkel

An Abstract of the Thesis Presented
in Partial Fulfillment of the Requirements for the
Degree of Master of Science
(in Quaternary and Climate Studies)
December 2016

Global climate reanalysis models are regularly used in many scientific fields concerning climate and atmospheric observation. This thesis utilizes reanalysis models in two chapters in order to gain insight into North Atlantic climate teleconnections and their relation to precipitation across South Greenland. This first chapter of this thesis compares the four most recent reanalysis models – ECMWF Reanalysis Interim (ERA-I), NCEP Climate Forecast System Reanalysis (CFSR), JMA 55-year Reanalysis (JRA-55), and NASA Modern-Era Retrospective Analysis for Research and Applications (MERRA) – and develops from these models a monthly-mean ensemble average of common meteorological variables for the period 1979-2013. Results from this analysis shows that the reanalyses are in good agreement above the friction layer in the atmosphere, whereas significant model differences are found near the surface. The second chapter of this thesis utilizes the previous results to investigate the relative importance of the North Atlantic Oscillation (NAO) (high-frequency atmospheric) and the Atlantic Multidecadal

Oscillation (AMO) (low-frequency sea-surface temperature) climate teleconnections as well as the Icelandic Low, Azores High, and blocking patterns in modulating precipitation across South Greenland. Key findings from this second chapter include: 1) years of extreme high and low precipitation in West Greenland are linked with the Icelandic Low, blocking patterns, and the westerly winds; and, 2) the long-term precipitation signal shows an increase of annual total precipitation and variability over southwest Greenland after the year 1995, suggesting an influence from the increase in both temperature and meridional flux of moisture and heat accompanied by a decrease in the zonal component of the westerlies. This work could be expanded upon in the future by identifying changes in synoptic fields during years of extreme high and low precipitation. Output from the four-member global climate reanalysis ensemble produced as part of this thesis will be made available online for community use.

ACKNOWLEDGEMENTS

I would like to first thank my advisor, Dr. Sean Birkel, for pointing me in directions I would not have gone before. My thought process and writing skill has changed by magnitudes due to him. I thank Dr. Paul Mayewski for guiding me through field research opportunities, such as Sweden and South Georgia Island. I would like to thank Dr. Kirk Maasch for brainstorming sessions and the many, deep conversations over good beer and garlic pizza. I also thank Dr. Keah Schuenemann for organizing my thoughts and reminding me of the days in Colorado.

This thesis work was supported by the National Science Foundation (NSF Award 1417640 to S. Birkel). My participation in Sweden during my graduate program was made possible by the Churchill Exploration Fund (advised by P. Mayewski). I thank Per Holmlund and Margareta Hanssen at the University of Stockholm for guiding the expedition on Mårmaglaciären, Sweden. I also thank Skip Novak and Capt. David Roberts and his crew for sharing knowledge on South Georgia Island and sailing the Southern Ocean.

I thank my officemates for all of the coffee breaks, outdoor lunches, long nights at local breweries, and for bringing in the many dogs of CCI. I thank Drs. Pascal Bohleber, Peter Koons, Bradfield Lyon, Andrew Carlton, Jasmine Saros, and Andrei Kurbatov for guidance on scientific topics either during meetings, farm work, or over gallons of IPA. And, I thank the 2016 Mandela Washington Fellows for giving me a change of pace.

Lastly, I thank my family for believing in me and pushing me further than I could have imagined. I thank my friends outside of UMaine for reminding me of the good old days. And to my partner, Dr. Franciéle Schwanck, you kept me sane and on track.

TABLE OF CONTENTS

LIST OF TABLES

LIST OF FIGURES

CHAPTER 1

INTRODUCTION

This thesis evaluates the performance of four leading global reanalysis models and then investigates linkages between atmospheric circulation over the North Atlantic and recent changes in precipitation in South Greenland. The work presented here is part of a broader National Science Foundation collaborative project between Dartmouth College, Boise State University, and the University of Maine called GreenTrACS (Greenland Traverse and Accumulation Studies), which aims to better understand changes in snow accumulation across West Greenland through the collection and analysis of shallow ice cores and evaluation against climate models.

In Chapter 2, I evaluate the four leading global climate reanalysis models and produce an ensemble average of several widely used meteorological outputs. Reanalysis refers to numerical models that calculate the state of the atmosphere at regular time intervals from interpolated input weather observations. Reanalysis models are increasingly used to study the evolution of Earth's atmosphere over the past several decades. The first global climate reanalysis model, NCEP/NCAR Reanalysis (NNR1; Kalnay et al., 1996), is on a course resolution of 2.5° x 2.5° latitude longitude grid with 28 vertical levels. Major improvements have been made since NNR1 related to data assimilation, internal physics, horizontal and vertical resolution, and availability of satellite data. The models evaluated here are the NCEP Climate Forecast System Reanalysis (CFSR; Saha et al., 2010), ECMWF Reanalysis Interim (ERA-I; Dee et al., 2011), JMA 55-year Reanalysis (JRA-55; Kobayashi et al., 2015), and NASA Modern-Era Retrospective Analysis for Research and Applications (MERRA; Rienecker et al.,

2011). As an important part of this work I have produced an ensemble average of all four models for 2-m air temperature, mean sea level pressure, precipitation, sea ice concentration, snow depth, sea surface temperature, total atmospheric water column, and wind speed/direction at the surface; as well as geopotential height, temperature, horizontal wind speed/direction, and vertical velocity (omega) over 6 pressure levels (1000, 925, 850, 700, 500, and 250 hPa). Comparison between the individual reanalysis models and the ensemble average shows significant differences in 2-m air temperature over the polar and desert regions, and in precipitation over coastal areas, high topography, and over the tropical Pacific Ocean.

In Chapter 3, I investigate linkages between South Greenland precipitation and the North Atlantic Oscillation (NAO), Atlantic Multidecadal Oscillation (AMO), Icelandic Low, Azores High, blocking patterns, near surface westerly winds, and temperature. The NAO describes the interannual variability of the meridional gradient of mean sea level pressure (MSLP) between the Icelandic Low and Azores High, whereas the AMO describes a ~70-year pattern of changes in sea surface temperature (SST) across the North Atlantic Basin. My investigation in this regard utilizes precipitation, MSLP, 2-m air temperature, and 10-m westerly wind fields from JRA-55. Given that Greenland is almost entirely covered by an ice sheet (~80%), there are very few locations where long-term weather observations have been recorded. One continuous record, however, is that of Nuuk, Greenland (64.2°N, 51.7°W), spanning 1958 – present. The Nuuk record is therefore used to evaluate the reliability of available reanalysis models. I find that precipitation output from JRA-55 (1958 – 2013) agrees well with Nuuk observations, and therefore use JRA-55 for the regional study. The JRA-55 precipitation averaged over

southwest Greenland shows a transition occurring around 1995, which coincides with the transition from the negative to positive AMO phase, the enhanced warming of the Arctic, and the recent decrease in the westerly zonal wind field. After 1995, the average annual precipitation total increases by ~9% in conjunction with an increase in standard deviation of ~60%. On a year-to-year basis, extreme precipitation events occur in concert with negative NAO-type patterns. For example, strong blocking patterns south of Iceland force cyclones to track poleward towards southwest Greenland, rather than to the southeast. In all, these results suggest that the interannual variability of precipitation over southwest Greenland is linked to the Icelandic Low and high pressure blocking patterns which is projected onto a long-wave frequency congruent with the AMO and the recent warming of the Arctic.

Chapter 4 of this thesis provides a summary of results and suggests avenues for further research.

CHAPTER 2

AN ENSEMBLE AVERAGE AND EVALUATION OF THIRD GENERATION GLOBAL CLIMATE REANALYSIS MODELS

2.1. Introduction

Reanalysis models are numerical frameworks from which gridded solutions for past atmospheric states are obtained from the assimilation of historical meteorological observations. The first such framework, NCEP/NCAR Reanalysis (NNR1; Kalnay et al., 1996), is a global model that provides meteorological outputs on a coarse 2.5° x 2.5° horizontal grid for the period of 1948 – present. A second generation of global climate reanalysis models, including ECMWF 40-year Reanalysis (ERA-40; Uppala et al., 2005) and JMA 25-year Reanalysis (JRA-25; Onogi et al., 2007), make improvements over NNR1 by integrating satellite data, cloud motion winds (ERA-40), and wind profiles around tropical cyclones (JRA-25) at a comparatively fine resolution of 1.125° x 1.125°. A third generation of global reanalysis models incorporate significant advances in data assimilation and internal physics, computed at resolutions less than 1° x 1°. These most recent models are NCEP Climate Forecast System Reanalysis (CFSR; Saha et al., 2010), ECMWF Reanalysis Interim (ERA-I; Dee et al., 2011), JMA 55-year Reanalysis (JRA-55; Kobayashi et al., 2015), and NASA Modern-Era Retrospective Analysis for Research and Applications (MERRA; Rienecker et al., 2011). These reanalyses span the 1979 – present satellite observation era, with the exception of JRA-55 which spans 1958 – present. Each of the third generation reanalysis models are considered state-of-the-art, but differences in meteorological outputs arise following different modeling approaches

(refer to Table 2.1 for general model comparisons; refer also to the "Overview & Comparison Tables" at https://climatedataguide.ucar.edu).

Reanalysis products are used increasingly for investigations into the changing climate. For example, Santer et al. (2004) find a trend of increasing tropopause heights in ERA-40 linked to anthropogenic-forced warming, in agreement with climate model simulations and satellite data. Serreze et al. (2012) compare vertical temperature and moisture profiles from CFSR, ERA-I, and MERRA to radiosonde station data within the Arctic, a data-sparse region where data interpolation is heavily simulated. They find good agreement between the reanalyses and measured temperature and moisture trends, even though uncertainties are produced in both radiosonde data and reanalyses. Lindsay et al. (2014) evaluated seven reanalysis models (at least one model per reanalysis generation) for the Arctic region and find that the third generation reanalyses (CFSR, ERA-I, and

Table 2.1 Major differences between each reanalysis model. For more information, see climatedataguide.ucar.edu/.

	CFSR	**ERA-I**	**JRA-55**	**MERRA**
Released	2010	2009	2013	2011
Output Resolution	0.5° x 0.5°	0.75° x 0.75°	0.562° x 0.562°	0.5° x 0.667°
Vertical Levels	64	60	60	72
Top of Atmosphere	0.266 hPa	0.1 hPa	0.1 hPa	0.01 hPa
Model Resolution	T382	T255	T319	0.5° x 0.667°
Data Assimilation	3DVAR	4DVAR	4DVAR	GEOS-5 IAU
Land Surface Scheme	Noah 4-Layer	Empirically	Simple Biosphere	Catchment LSM
Radiation Scheme	RRTMG	RTTOV v7	RTTOV v9.3	CRTM
Output Formats	GRIB	GRIB/netCDF	GRIB	HDF/netCDF

MERRA) provide the most significant correlations to observations, but with biases between the reanalyses for 2-meter air temperature and other metrics. Chen et al. (2014) examine variability between CFSR, ERA-I, JRA-55, and MERRA in the warm-season diurnal cycle over East Asia. They find that although these four reanalysis models reproduce the diurnal precipitation well over large spatial scales, individual models disagree considerably over regional scales. Chen et al. also show that JRA-55 is in good agreement with observational data showing an increase in morning precipitation over their investigated domain. This same study determines that JRA-55 accurately reproduces wind speeds on the leeside of the Tibetan Plateau.

The above reanalysis evaluations can be referred to as model-observation comparisons, because the models are compared directly against station, radiosonde, and satellite data. Here, we take a different approach and present an ensemble average and model intercomparison of the four leading reanalysis models, CFSR, ERA-I, JRA-55, and MERRA. In this work we examine differences between the ensemble average and individual ensemble members for 2-meter air temperature over land (T_{2m}), precipitation, and 500-hPa geopotential height (Z_{500}). Comparisons are made against the present 30-year climate normal (or average) spanning 1981 – 2010. Our analysis shows that ensemble-member interannual variability correlations are significant throughout, but considerable differences exist between the reanalyses, particularly for T_{2m} over desert areas where moisture availability is low, as well as regional precipitation.

2.2. Data and Methods

Output from CFSR, ERA-I, and JRA-55 models were obtained from the NCAR Computational Information Systems Laboratory (CISL) Research Data Archive (RDA; http://rda.ucar.edu) under ds093.0, ds627.1, and ds628.1, respectively. Output is available in monthly means for ERA-I and JRA-55. CFSR monthly means are not available through CISL, and therefore it was necessary to generate monthly means by averaging the available 3-hourly outputs (00, 06, 12, 18 UTC and the 3-hour forecasts associated with each time step). Monthly mean files for MERRA were obtained from the NASA Modeling and Assimilation Data and Information Services Center (MDISC; http://disc.sci.gsfc.nasa.gov/mdisc).

The unprocessed outputs for each reanalysis model in this study are on different horizontal grids (Table 2.1). For simplicity, all model output fields were regridded to the same regular 0.5° x 0.5° latitude-longitude grid used by CFSR. Regridding was done using bilinear interpolation from the Earth System Modeling Framework (ESMF) software embedded within NCAR Command Language (NCL). Once regridded, netCDF files were produced for monthly, seasonal, and annual averages for each year and reanalysis product (refer to the Appendix for code). The 1981 – 2010 climate normal was generated, again, for each month, season, and year. The reanalysis ensemble was generated by averaging monthly, seasonal, and annual means of the meteorological fields defined above across all four models, CFSR, ERA-I, JRA-55, and MERRA.

Figure 2.1Two-meter air temperature differences. (a-d) Gridded differences in 2-meter air temperature for each reanalysis model subtract (e) the ensemble average 2-meter air temperature. Black boxes show locations for annual average time series in Fig. 2.2.

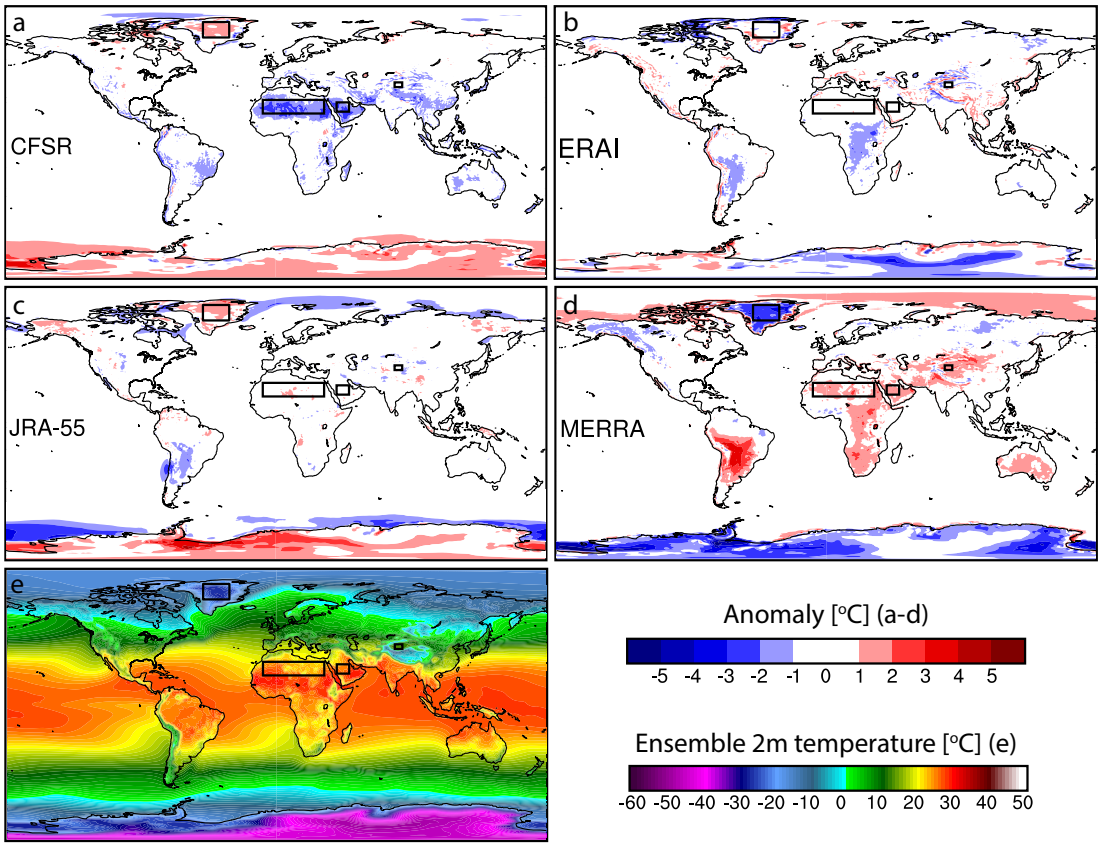

2.3. Results

2.3.1. Two-meter Air Temperature

Global, land-based 2-meter air temperature (T_{2m}) anomalies (Fig. 2.1) arise primarily near the poles, with slight departures from the ensemble average, generally in locations where moisture content is either low (deserts) or high (rainforests). For example, CFSR affords a negative 2 – 3°C difference over the desert belts in Africa and the Middle East (i.e. Sahara, Sahel, and Saudi Arabia), while ERA-I shows most differences, about -1°C, in central South America and central Africa, locations of large tropical rainforests. From JRA-55, T_{2m} compares well with the ensemble average overall but with a negative difference in northern Chile. Last, from MERRA, T_{2m} is generally warmer than the ensemble average over Africa, Australia, and South America.

Time series of T_{2m} during the 30-year period over desert regions (black boxes in Fig. 2.1) can be seen in Fig. 2.2. Interannual variability between the reanalyses agree well for each region ($r > 0.8$). The range of time series correlations across the smallest desert, the Taklimakan Desert, China, is larger ($0.85 < r < 0.97$) than that of the correlation coefficient ranges for the Sahara Desert, Saudi Arabia, and Central Greenland ($0.94 < r < 0.99$, $0.91 < r < 0.99$, and $0.91 < r < 0.98$, respectively). The topography surrounding the Taklimakan Desert differs much more than that of the other deserts referred to here, which could explain the variability in differences found between the reanalyses.

Figure 2.3 shows the time series for T_{2m} over the ensemble record, 1979-2013, and correlation coefficients. Note that all reanalysis-ensemble correlations are greater than 0.95. Reanalysis-reanalysis T_{2m} correlations are also high, with the lowest being between CFSR and JRA-55 at 0.88. ERA-I shows the highest correlation against the

Figure 2.2 Two-meter air temperature differences over deserts. Times series of each member and ensemble average (GEN3) of annual 2-meter air temperature averaged over the 1981-2010 period. Locations shown as black boxes in Fig. 2.1.

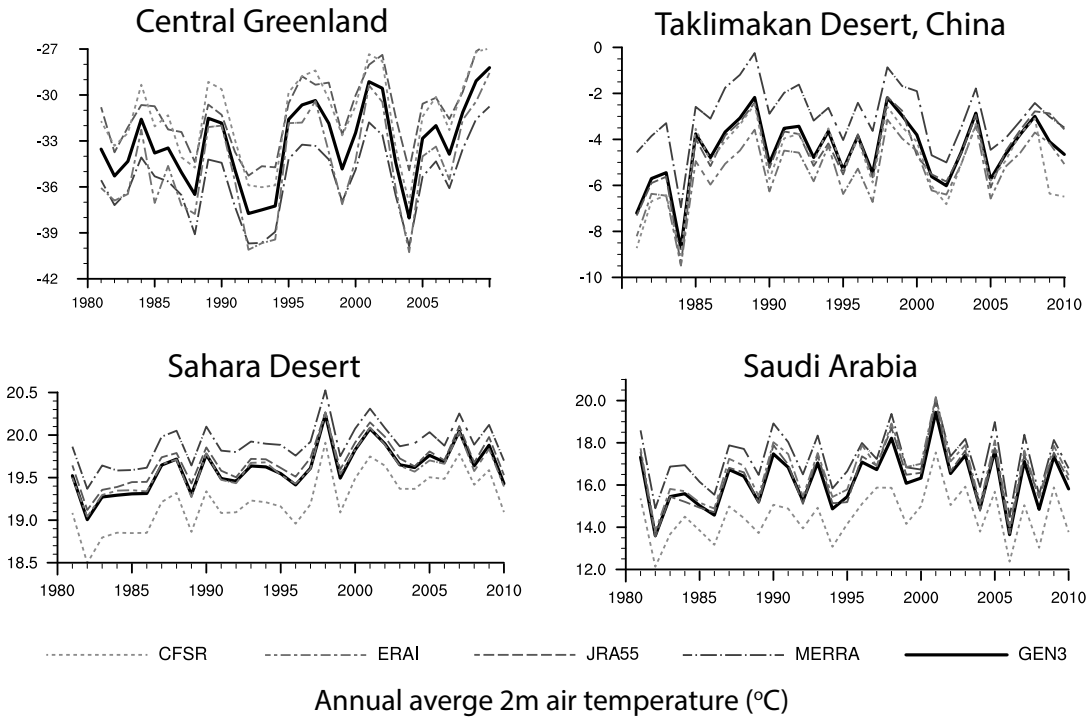

Figure 2.3 Global annual 2-meter air temperature for each member and the ensemble (GEN3) average from 1979 – 2013. Correlation coefficients (r) for each time series shown in upper, left table.

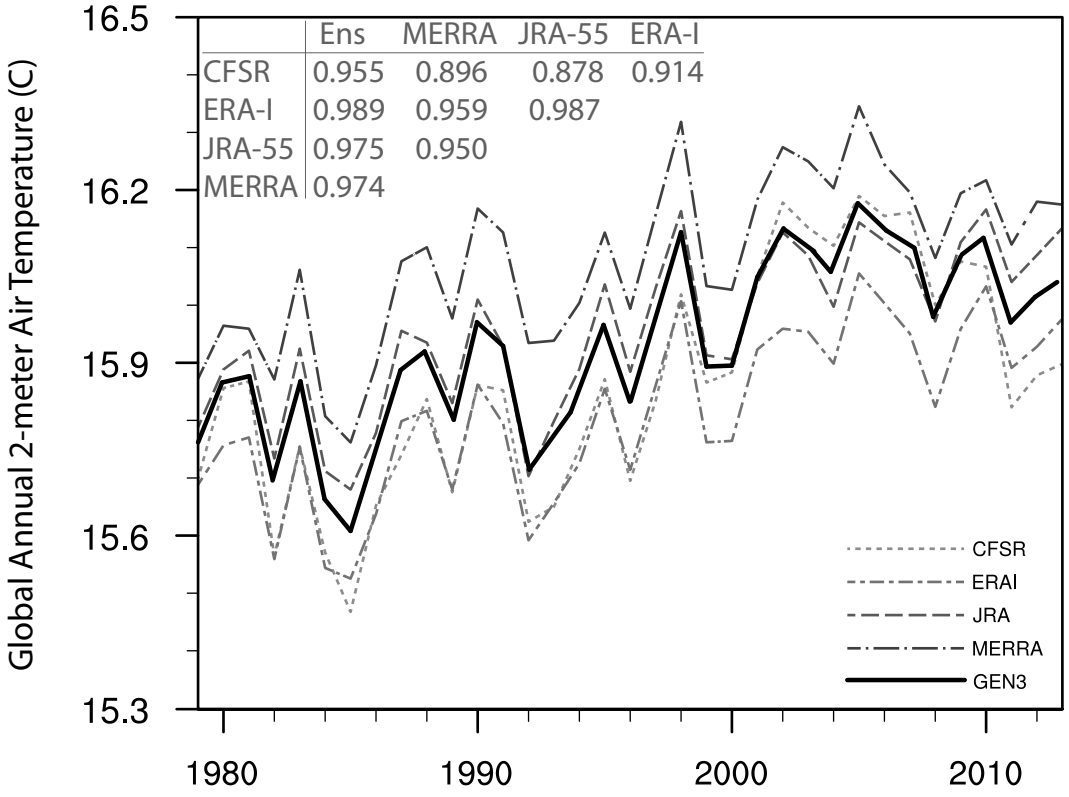

Figure 2.4 Winter two-meter air temperature differences. (a-d) The boreal winter (DJF) 2-meter air temperature anomalies of (e) the winter ensemble average.

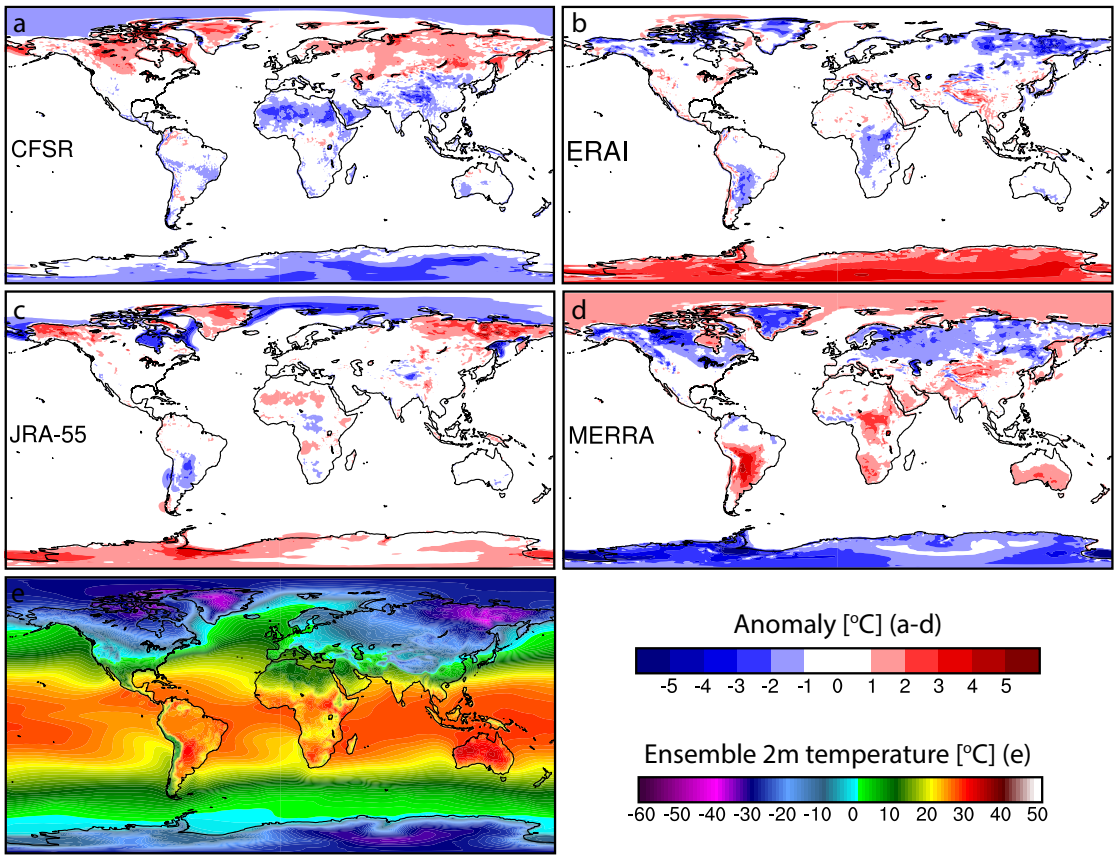

Figure 2.5 Summer two-meter air temperature differences. (a-d) The boreal summer (JJA) 2-meter air temperature anomalies of (e) the summer ensemble average.

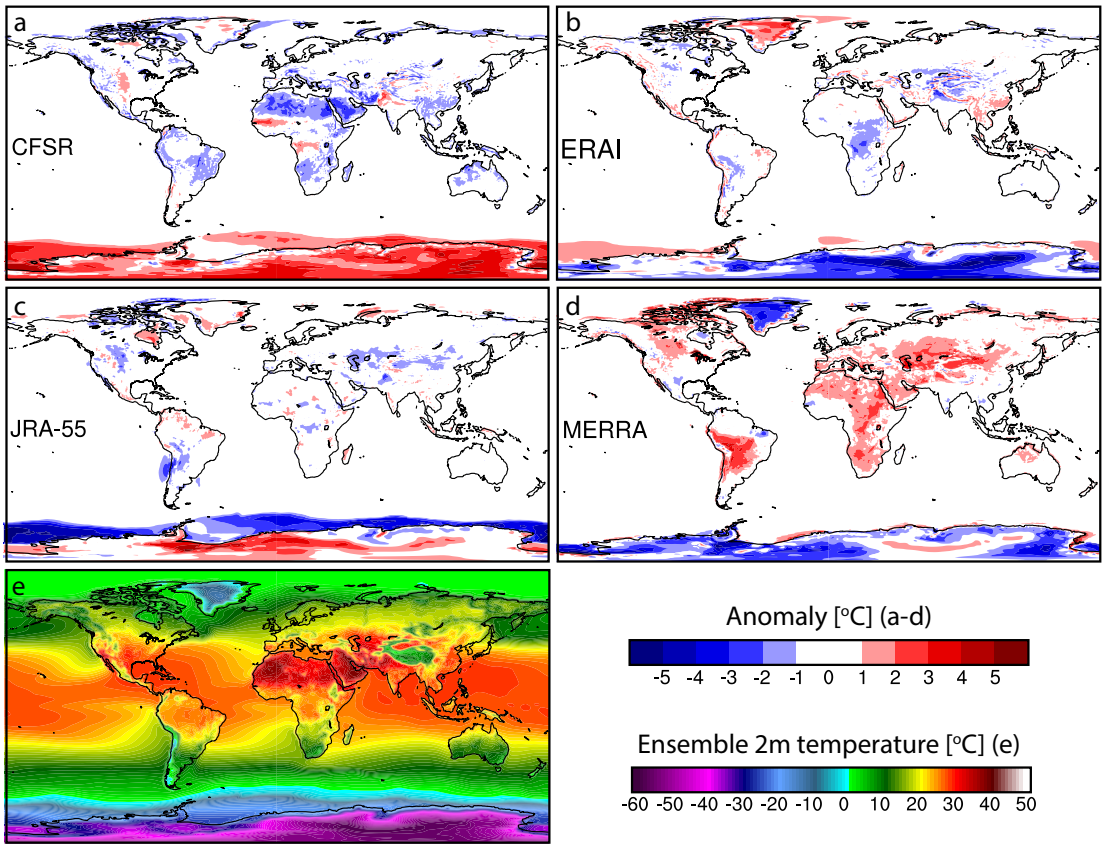

ensemble average at 0.99 though the ERA-I T_{2m} has a difference of about -0.10°C compared to that of the ensemble average. MERRA T_{2m} has the highest average deviation from the ensemble of about +0.14°C. The MERRA T_{2m} time series curve does not intersect the other reanalysis curves making MERRA outputs anomalously warmer each year with respect to each reanalysis. The JRA-55 T_{2m} time series is closest to the ensemble average with a mean departure of about -0.02°C. For boreal winter (DJF) and summer (JJA) differences, refer to Figs. 2.4 and 2.5, respectively.

In order to compare T_{2m} trends, the derivative of 5-year running means is used for each reanalysis model. ERA-I, JRA-55, and MERRA display similar trends across the 1979 – 2013 period. However, CFSR yields a steeper increase in T_{2m} during the 1997 – 2003 period and a steeper decline across the 2007 – 2013 period relative to ERA-I, JRA-55, and MERRA. The CFSR T_{2m} increase over the first period is 0.061 °C/yr whereas the other reanalysis trends are less than 0.038 °C/yr. The CFSR decrease over the latter period is -0.036 °C/yr whereas ERA-I, JRA-55, and MERRA show a range of trends (between -0.010 and 0.003 °C/yr).

For ocean-based 2-meter air temperature, the reanalyses generally agree well with the ensemble average, which is to be expected as each reanalysis uses a prescribed SST field interpolated from observations. CFSR additionally incorporates a combination of versions 1 and 2 of the optimum interpolation (OI) methods for the period November 1981 – present (Reynolds et al., 2007) with SST fields prepared for ERA-40 used over the January 1979 – October 1981 period. For further information on reanalyses and SST data sets and methods for CFSR, ERA-I, and MERRA, refer to Kumar et al. (2014). JRA-

55 uses the Centennial in situ Observation-Based Estimates (COBE) SST data set (Hirahara et al. 2014).

2.3.2. Precipitation

Difference plots similar to Fig. 2.1 for precipitation between the reanalyses used in this study and the ensemble average are undoubtedly noisy, notably along mountain ranges (e.g. Rocky Mountains and Himalayas) and near small islands (e.g. Philippines). In the western hemisphere tropics, the inter-tropical convergence zone (ITCZ) is clearly seen in the zonal averages of yearly precipitation over the 1981-2010 climate average (Fig. 2.6). Precipitation outputs from CFSR and ERA-I in this region generally agree with the ensemble average, whereas JRA-55 and MERRA deviate from the ensemble average on the order of 0.42 and -0.68 m/yr, respectively, at the peak of the zonal average. JRA-55 presents a much stronger precipitation belt while the zonal average from MERRA suggests a weaker zonal average, with respect to CFSR and ERA-I. Seasonal differences relative to the ensemble average arise during the boreal summer (JJA) and fall (SON) months for JRA-55 and MERRA. The reanalysis models have poor agreement on the precipitation total in the ITCZ, but good agreement overall on timing of the seasonal shift of the ITZC in the Pacific Ocean. The zonal average peaks for each reanalysis model fall within 1° latitude of the ensemble zonal average peak.

CFSR exhibits a specific weakness not found in the other models, that is the occurrence of spherical harmonic artifacts in at least the precipitation (Fig. 2.7) and T_{2m} fields. These unrealistic features are not only found in sub-daily and monthly outputs, but also present in the climatological average, 1981 – 2010. Slight spherical harmonic

Figure 2.6 Precipitation zonal average differences over western hemispheric tropics. (a) The average total annual precipitation over the 1981 – 2010 average for the western hemispheric tropics. The black curve in (b) is the ensemble zonal average of precipitation from (a). The black curves in (c-f) are the respected precipitation zonal average over the same region as (a). The gray curves in (c-f) show the differences of the ensemble subtracted from the reanalysis model. The thin black line in (c-f) marks zero difference.

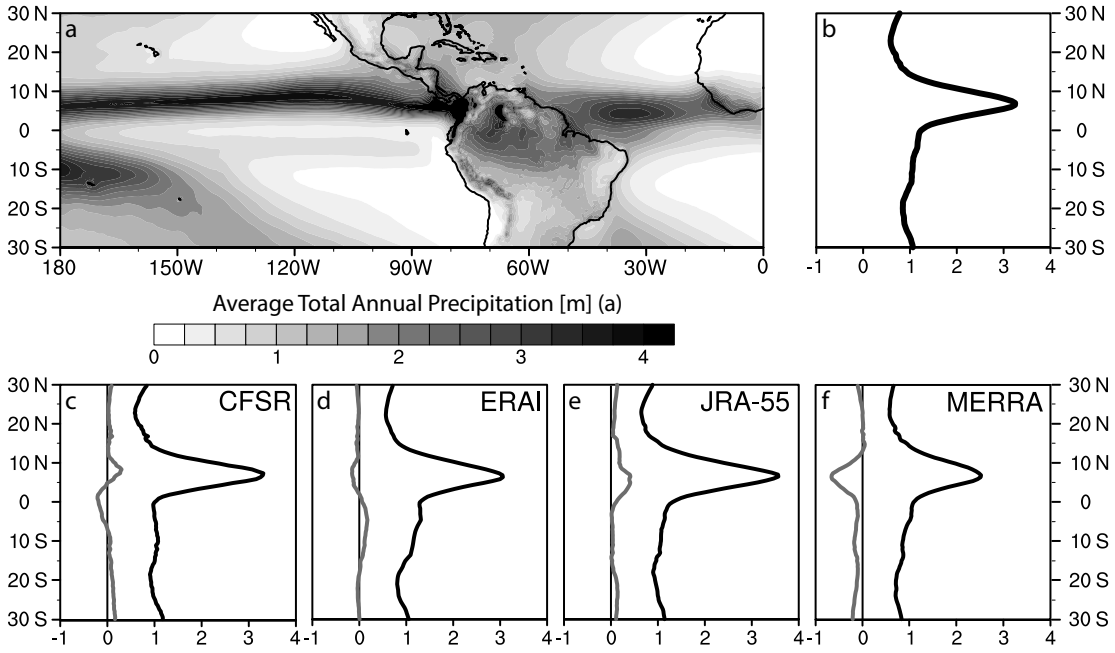

artifacts in T_{2m} and precipitation are present within the ensemble average produced here as a result of the inclusion of CFSR.

2.3.3. 500-hPa Geopotential Height

Geopotential height outputs at 500 hPa (Z_{500}) agree across the four reanalyses with slight differences (+/-20 m) (Fig. 2.8). The largest deviations are over Antarctica, where radiosonde observations are sparse, and therefore the models are poorly constrained. Above the friction layer, the free atmosphere becomes geostrophic, enabling model simulations to better approximate real-world observations. However, it is expected that higher Z_{500} occur over regions where reanalyses show higher surface temperature, due to thermal expansion; this pattern is not found. Z_{500} over Antarctica, for example, are lower (higher) for CFSR and JRA-55 (ERA-I and MERRA) (Fig. 2.8) and display relatively higher (lower) T_{2m} (seen in Fig. 2.1).

2.4. Conclusion

In conclusion, three widely used atmospheric variables – T_{2m}, precipitation, and Z_{500} – are compared between each of the third generation global climate reanalysis models – CFSR, ERA-I, JRA-55, and MERRA – and the respective ensemble average of these reanalyses. While the four products generally agree on the large-scale and above the friction layer, there are differences when examining regional-scale climatology and variables within the friction layer. For example, T_{2m} outputs for each reanalysis are shown to have large differences in extremely dry regions, such as polar ice sheets and low-latitude deserts. T_{2m} over the Sahara, Sahel, and Saudi Arabia in CFSR (MERRA) is

Figure 2.7 A comparison between CFSR (top) and ERA-I (bottom) 1981 – 2010 average yearly precipitation totals. CFSR contains unrealistic, harmonic spherical artifacts on short and long term averages whereas ERA-I (as well as JRA-55 and MERRA) displays a more realistic output.

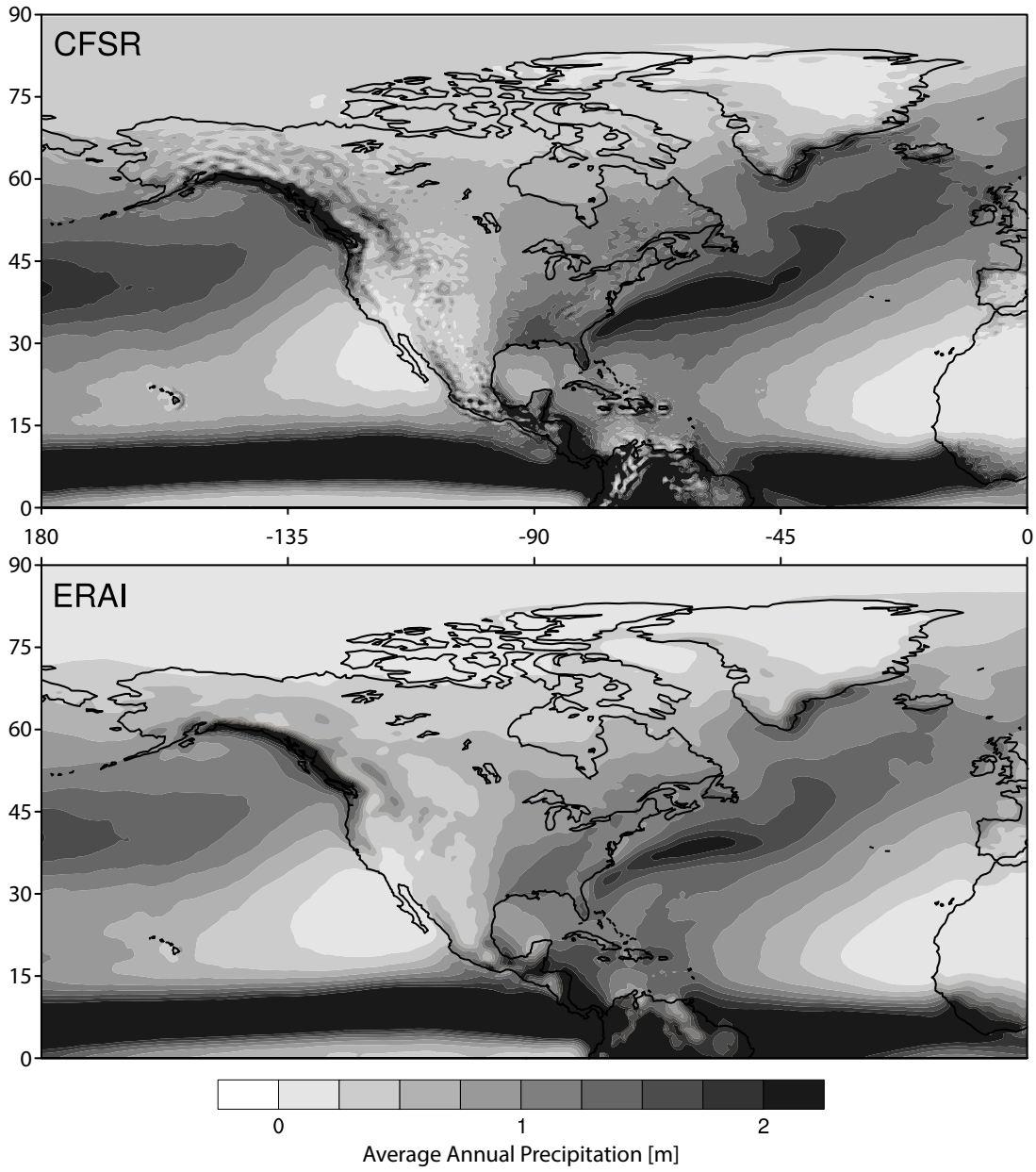

Figure 2.8 Geopotential height differences at 500 hPa. (a-d) The difference of 500-hPa geopotential heights between the reanalysis and (e) the ensemble, reanalysis subtract the ensemble. Horizontal-line artifacts in maps (a-d) are inherited from regridding within MERRA.

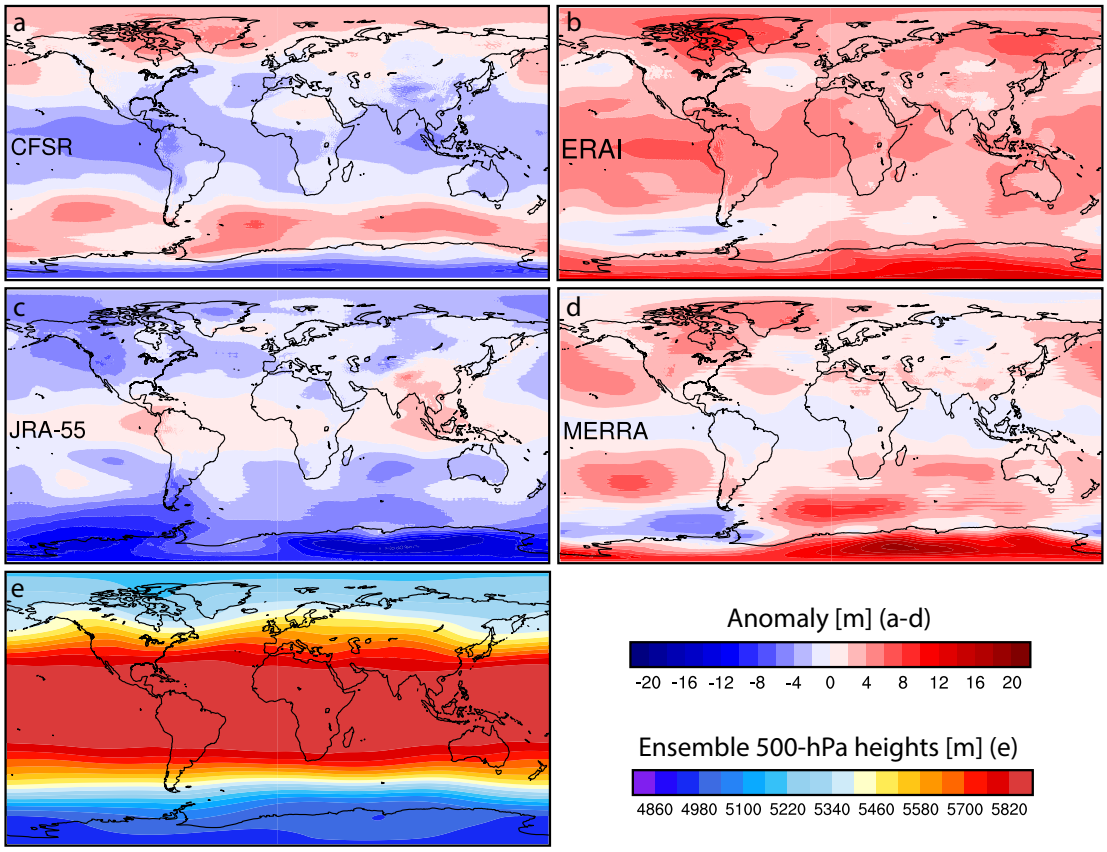

much lower (higher) with respect to the ensemble average during the period 1981-2010, whereas ERA-I and JRA-55 are generally in good accord with the ensemble (Figs. 2.1 and 2.2). Differences in these areas are most likely linked to scarce observational data. T_{2m} correlations between the reanalysis models reveal strong agreement (Fig. 2.3) for interannual variability, meaning that the models are in agreement on large-scale circulation processes and likely radiation schemes. For precipitation, we note that the ITCZ precipitation belt display differences between model solutions on the order of 20% (i.e. MERRA) relative to the ensemble average.

Although, differences near the surface arise between the reanalysis model solutions, which could be attributed to any number of internal model differences, such as resolution, assimilation methods, observational error, land surface schemes, physics, etc. Future work on meteorological case studies will prove useful for improving daily and sub-daily reanalysis outputs within the next generation of reanalysis products. Since most reanalysis differences occur at or near the surface, investigating the internal models and surface model schemes will bring reanalysis solutions closer to observations.

CHAPTER 3

EXAMINATION OF PRECIPITATION VARIABILITY IN SOUTH GREENLAND

3.1. Introduction

The Greenland Ice Sheet contains the equivalent of ~6.7 m of global sea level and constitutes a laterally extensive, high albedo surface that impacts the Northern Hemisphere radiation balance by reflecting ~70% of the local incoming solar radiation (Ohmura and Reeh, 1991; Tedesco et al., 2015). The identification of atmospheric teleconnections that modulate moisture and heat transport to the ice sheet can improve future climate projections.

This study utilizes the Japanese Meteorological Agency (JMA) 55-year Reanalysis (JRA-55; Kobayashi et al., 2015) model to evaluate dominant atmospheric circulation patterns that control precipitation delivery to South Greenland, and therefore have an impact on the overall mass balance of the ice sheet and future sea level rise. We first provide the climate of Greenland then discuss the interannual variability of precipitation in southwest and southeast Greenland. We focus the study on meteorological variables that influence ice sheet mass balance: surface temperature, mean sea level pressure, and surface wind, with a particular focus on precipitation. As these variables are strongly linked with known climate oscillations in the North Atlantic, we consider linkages between temperature, wind, and precipitation and local climate indices, the North Atlantic Oscillation (NAO) and Atlantic Multidecadal Oscillation (AMO).

3.1.1. South Greenland and North Atlantic Climate

Our examination of the atmospheric patterns linked with South Greenland precipitation involves a survey of diagnostic meteorological metrics. Two-meter air temperature (T_{2m}; Fig. 3.1a), mean sea level pressure (MSLP; Fig. 3.1b), 10-m u (zonal) and v (meridional) winds (u_{10m}, Fig. 3.1c; and v_{10m}; Fig. 3.1d), and precipitation (Fig. 3.1e) in South Greenland are heavily impacted by the topographic divide of the ice sheet, a ridge along the 44°W longitude. The high altitude surface of the Greenland ice sheet induces strong anticyclonic katabatic winds during winter months, known as the Greenland High, and serves as a topographical barrier that facilitates large hydraulic jumps and the formation of lee-side troughs over the Denmark Strait (Doyle et al., 2005). The longitudinal ridge is prominent enough to create two major climate regimes. Temperature is coldest along the ridge and increasing toward the coastline with a shallower T_{2m} gradient to the west, and a steeper gradient to the east. Flow across southwest Greenland is dominated by comparatively dry southeasterly winds, whereas flow across the southeast is dominated by moist northwesterly winds. These wind patterns can be explained by the climatological Greenland High anticyclone (orange center in Fig. 3.1b).

Figure 3.2 shows the interannual variability of total annual precipitation in both southwest (gray) and southeast (black) Greenland as modeled by JRA-55. These precipitation signals differ both in interannual variability and in long-term trends ($p < 0.05$). Total annual precipitation and interannual variability of the signal increase from 1970 to 2013 whereas southeast Greenland shows an increase in variability from about 1970 to 1990, with a general decrease in interannual variability to 2000. The amount of

Figure 3.1 Greenland climatology showing 2-m air temperature (a), mean sea level pressure (b), 10-m u-winds (c), 10-m v-winds (d), and precipitation (e) averaged over the JRA-55 record, 1958-2013.

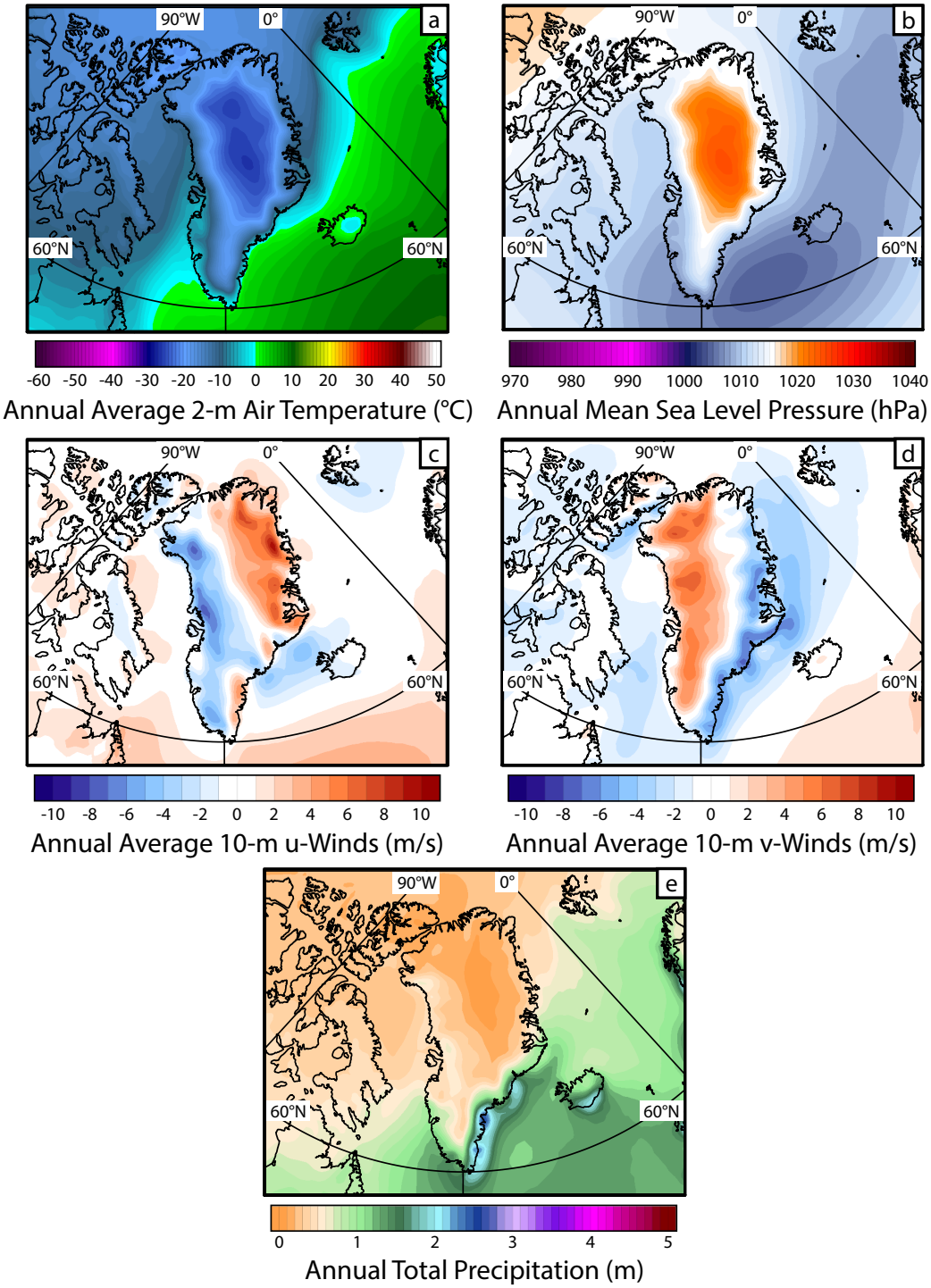

Figure 3.2 Southwest (gray) and Southeast (black) precipitation output from JRA-55.

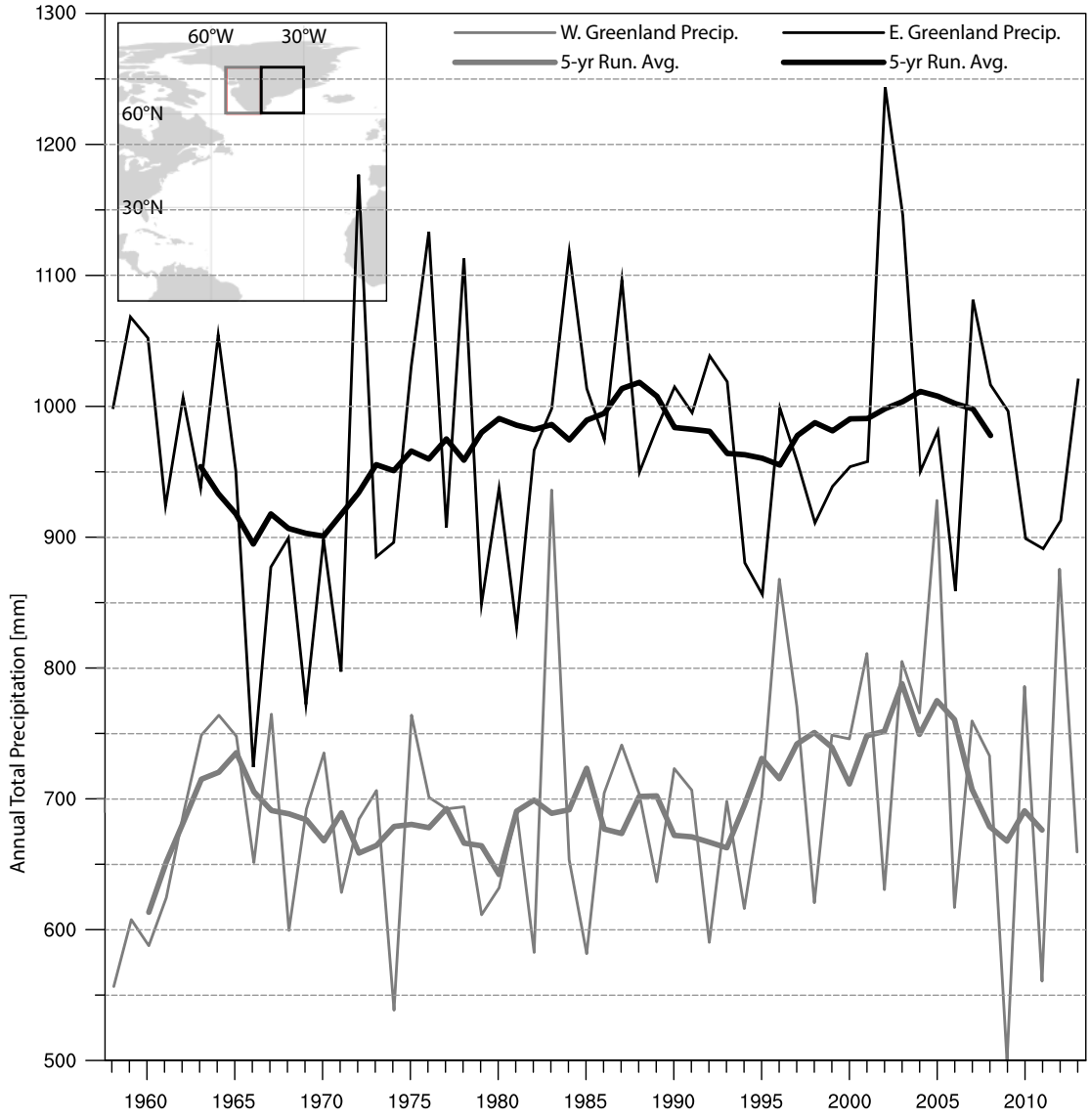

total annual precipitation is greater in the southeast with respect to the southwest by upwards of 2000 mm/year in some localized areas (Fig. 3.1e), and over 200 mm/year across the southwest and southeast regions (Fig. 3.2). Southeast Greenland receives more precipitation during the winter (DJF; ~200 mm/year), spring (MAM; ~75 mm/year), and autumn (SON; ~55 mm/year) months, with respect to the southwest. During the summer (JJA) months, southeast Greenland receives slightly less precipitation than the southwest (~30 mm/year). The higher amount of annual precipitation in southeast Greenland is due to the increased number of cyclones that expire in the Icelandic region rather than over the Labrador Sea. The month, season, and year averages of low pressure systems in the North Atlantic is called the Icelandic Low (blue center in Fig. 3.1b), due to the general Icelandic location of the climatological low pressure center. The Icelandic Low is one of two poles that make up the derived climate index, the North Atlantic Oscillation (NAO; Fig. 3.3), which is described in the following.

The NAO is defined as the fluctuation in the meridional gradient of the MSLP fields between Iceland and the Azores Islands. The phenomenon was named by Walker and Bliss (1932, first mentioned by Walker, 1923) who described the NAO as the tendency of the coordinated strengthening or weakening of the Icelandic Low and the Azores High, climatological features seen in monthly, seasonal, and annual MSLP fields in the North Atlantic. A strengthening of the Icelandic Low and Azores High creates a tighter meridional MSLP gradient (+NAO) accompanied by increased near-surface winds, whereas a weakening forms a weaker meridional MSLP gradient (-NAO) accompanied by weaker near-surface winds. Rogers (1990) connects MSLP patterns in the North Atlantic to cyclone tracks and finds that during extreme +NAO years, the

Icelandic Low is deeper and east of South Greenland leading to a strong MSLP gradient, which he links to the meridional cyclone frequency gradient. Conversely, during extreme -NAO years, the center of highest cyclone frequency (Icelandic Low) is located farther southwest, off the U.S.A. northeast and Nova Scotia coasts. Serreze et al. (1997) find an increase of cyclone frequency (over 2 times) and intensity during +NAO years when compared to -NAO years.

There is also another climate index located in the North Atlantic that may be linked to precipitation in South Greenland: the Atlantic Multidecadal Oscillation (AMO; Fig. 3.3). The AMO is a well-known climate pattern in the North Atlantic, but is not as well understood as the NAO. The AMO index describes the multi-decade variation of sea surface temperature (SST) in the North Atlantic Basin, a phenomenon first identified by Schlesinger and Ramankutty (1994). Enfield et al. (2001) define the AMO index as the linearly detrended, 10-year running mean of SST anomalies with respect to the 1856-1999 mean using the Extended Reconstructed SST (ERSST; Kaplan et al. 1998) gridded dataset. Wunsch (1992) notes that a widespread North Atlantic basin SST oscillation is difficult to claim as driven by internal forces based on the sparse observational data from the oceans. Despite this, the AMO is widely suggested to originate from variations in the Atlantic Meridional Overturning Circulation (AMOC), a phenomenon through which thermohaline circulation, driven by density gradients due to temperature and salinity (Delworth and Mann 2000), and buoyancy forcing, driven by density differences due to freshwater input (Otterå et al. 2010), are thought to provide the key driving stress for the northeastward flow of the Gulf Stream. Wunsch and Ferrari (2004) clearly describe ocean circulation and mixing as controlled by wind. Furthermore, Wunsch (2006) argues that in

order to solve for the net meridional property flux (equation 2 in manuscript), the variables needed are not resolved in the current climate models. Clement et al. (2015) simulate an atmospheric general circulation model coupled to a 50 m thick slab-ocean model. They find that the simulated North Atlantic SST variations closely resemble those found in the AMO, thus concluding that ocean circulation is less influential to the SST, thus the AMO index. Similarly, Birkel and Mayewski (2015) ascribe the origin of the AMO to a wind-stress forcing that develops following major volcanic eruptions. Their claim is deduced from the strong coincidence between measurements of high stratospheric aerosol content and cool SSTs. Birkel and Mayewski show that SSTs in the North Atlantic subpolar region south of Greenland (beneath the westerly wind belt) co-vary with 10-meter wind speeds, and also the strength of the West African Monsoon, together implying a basin-wide atmospheric link.

3.2. Data and Methods

3.2.1. Atmospheric Reanalysis

We begin our analysis of South Greenland precipitation by first validating the JRA-55 modeled precipitation to observations in Nuuk, Greenland. Weather observations over Greenland are sparse, and therefore efforts here are primarily dependent on utilizing output from gridded climate reanalyses. Of the several available reanalysis models, we use JRA-55 because it provides the longest record of all available third generation reanalyses (NCEP/NCAR CFSR, ECMWF Reanalysis Interim, and NASA MERRA start in 1979 whereas JRA-55 begins in 1958) and also proves to reliably reproduce monthly and yearly total precipitation observations at Nuuk, Greenland, as demonstrated later in

this paper. When first released, JRA-55 spanned the years 1958 (following the International Geophysical Year, beginning of continuous global radiosonde observations) to 2012. As of the time of this analysis, JRA-55 has been extended to 2013. Monthly output for JRA-55 was obtained from the NCAR Computational Information Systems Laboratory (CISL) Research Data Archive (RDA; http://rda.ucar.edu) under ds628.1, as found on the Yellowstone supercomputer.

3.2.2. Nuuk, Greenland Observations

Weather station records in South Greenland commonly span only 5 – 10 years. Observations from Nuuk, however, contain a near-continuous record of precipitation spanning 1958 – present with only 151 days of missing precipitation data out of the total 20,454 days, 0.7% of the record between 1958 – 2013. Of the 151 missing points, 69 are missing from January 1 to April 30, 2013, whereas the remaining 82 missing points are spread evenly across the remainder of the data record, with less than 3 data points missing in a given month. Other long precipitation records in South Greenland contain large gaps on the order of 20 - 40% of missing daily precipitation observations. The daily Nuuk precipitation observations are obtained from the Global Historical Climatology Network (GHCN) at NOAA National Centers for Environmental Information (NCEI). For this paper, the daily precipitation amounts are summed into year (Fig. 3.3) and month (Fig. 3.4) totals.

Figure 3.3 Nuuk, Greenland precipitation observations (black) and JRA-55 precipitation output over Nuuk (gray) in mm per year.

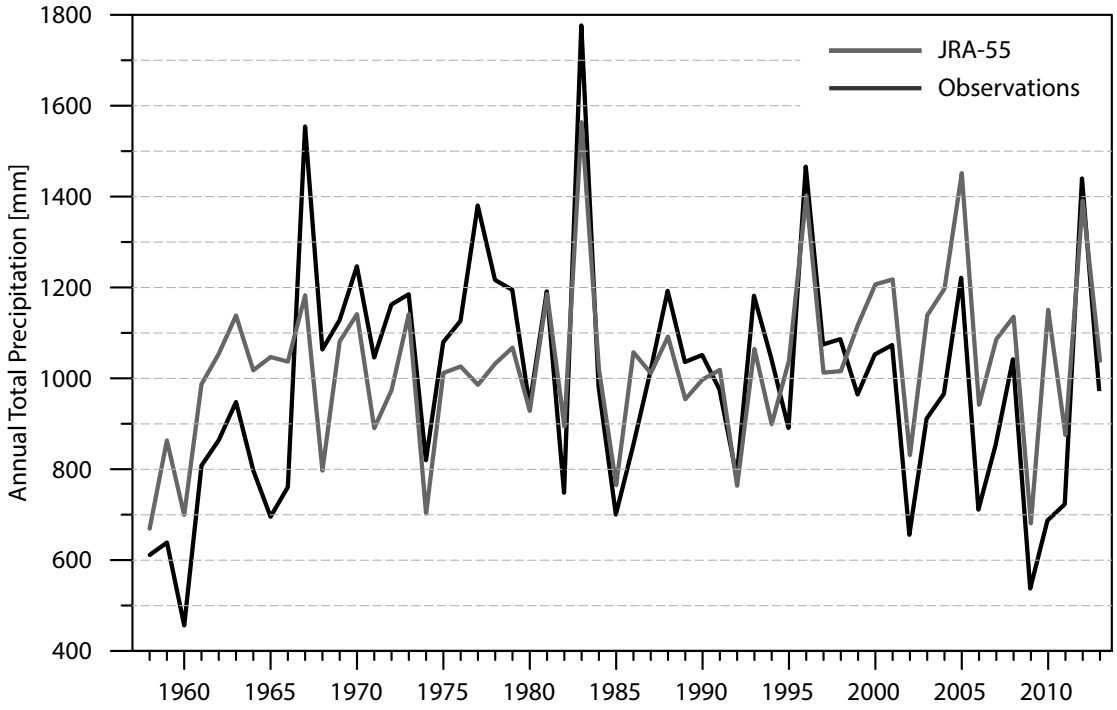

Figure 3.4 Nuuk, Greenland precipitation observations (black) and JRA-55 precipitation output over Nuuk (gray) in mm per month.

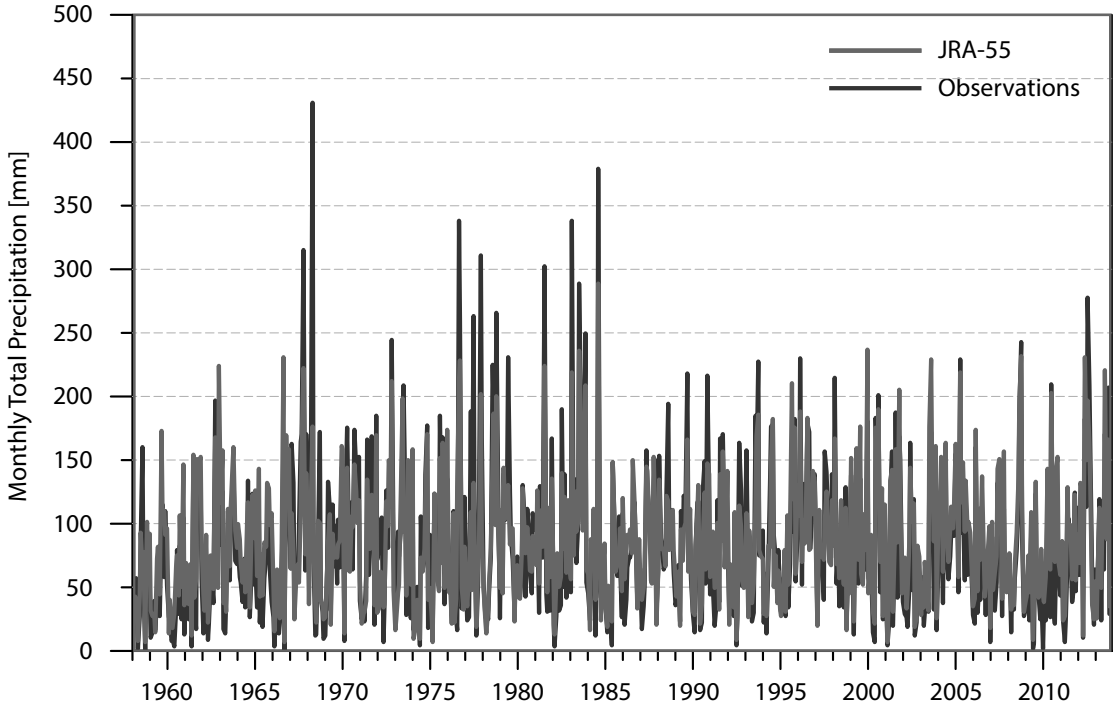

3.2.3. Reanalysis Validation

JRA-55 precipitation was validated by correlating to Nuuk observations. As we are comparing a point observation to gridded model output, the comparison is better suited for temporal averages (Ensor and Robeson, 2008), year and month totals. Year totals compare well against JRA-55 output ($r = 0.72$). As seen in Fig. 3.3, the correlation preceding 1979 is much lower than that of the years following 1979 ($r = 0.60$ and 0.81, respectively). Thus, the integration of satellite data from 1979 onwards has, as expected, added significant confidence with respect to the interpretation of precipitation in JRA-55, at least over this location. Monthly precipitation totals correlate very well with JRA-55 output over Nuuk, Greenland ($r = 0.86$), but unlike the year totals, the correlation coefficient does not increase as dramatically from before to after 1979 ($r = 0.84$ and 0.89, respectively).

Less precipitation falls during winter and early spring months with an increase of precipitation during late summer and fall months. The decreased precipitation during winter months is partly due to the Greenland High, as mentioned earlier, which blocks low pressure centers (storms) from traversing much of Greenland. The Greenland High is most prominent during winter months due to extreme katabatic flow from a lack of local incoming solar radiation, i.e. constant, cold, dense air flowing from high to low elevations. As JRA-55 captures seasonality seen in the observations, the monthly correlation coefficient is improved over the yearly correlation.

Table 3.1 shows the 56-year total precipitation bias between Nuuk observations and JRA-55 output to be about 2 meters. The JRA-55 precipitation output is higher than that of the observed precipitation, an average difference of 36 mm/year or 3 mm/month.

Table 3.1 Nuuk, Greenland precipitation observations subtract JRA-55 model output general statistics for monthly and yearly totals in mm. All month and year totals are rounded to nearest mm.

	Minimum	Maximum	Mean	Mode (times)	Standard Deviation	Total Diff.
Monthly	-122	255	-3	-14 (21)	30	-2013
Yearly	-462	397	-36	-152 (2)	177	-2002

3.2.4. Indices

The NAO (Fig. 3.5) index used here explains two climatological pressure centers, the Icelandic Low and Azores High, which can be seen in the leading empirical orthogonal function (EOF) of the Northern Hemisphere MSLP anomalies, explaining 42.8% of the DJFM variance (Hurrell 2003). Although the NAO describes the winter MSLP gradient, the gradient does exist, albeit more subdued, during the rest of the year and can be seen in the leading EOF of MSLP through the other seasons (MAM, JJA, and SON). The variance explained by the first EOF decreases through the seasons (MAM, 33.6%; JJA, 27.9%; and SON, 22.6%) with the annual anomaly variance explained at 32.4% (Hurrell, 2003). This EOF-based NAO index and EOF information can be found at the NCAR UCAR Climate Data Guide website (https://climatedataguide.ucar.edu/climate-data/hurrell-north-atlantic-oscillation-nao-index-pc-based).

The AMO index used here (Fig. 3.5) is built from a similar method to that of Enfield et al. (2001) with a few changes. The annual North Atlantic SST anomalies used

Figure 3.5 NAO (black) and AMO (gray) Indices (thin lines) with their 5-year running means (thick lines).

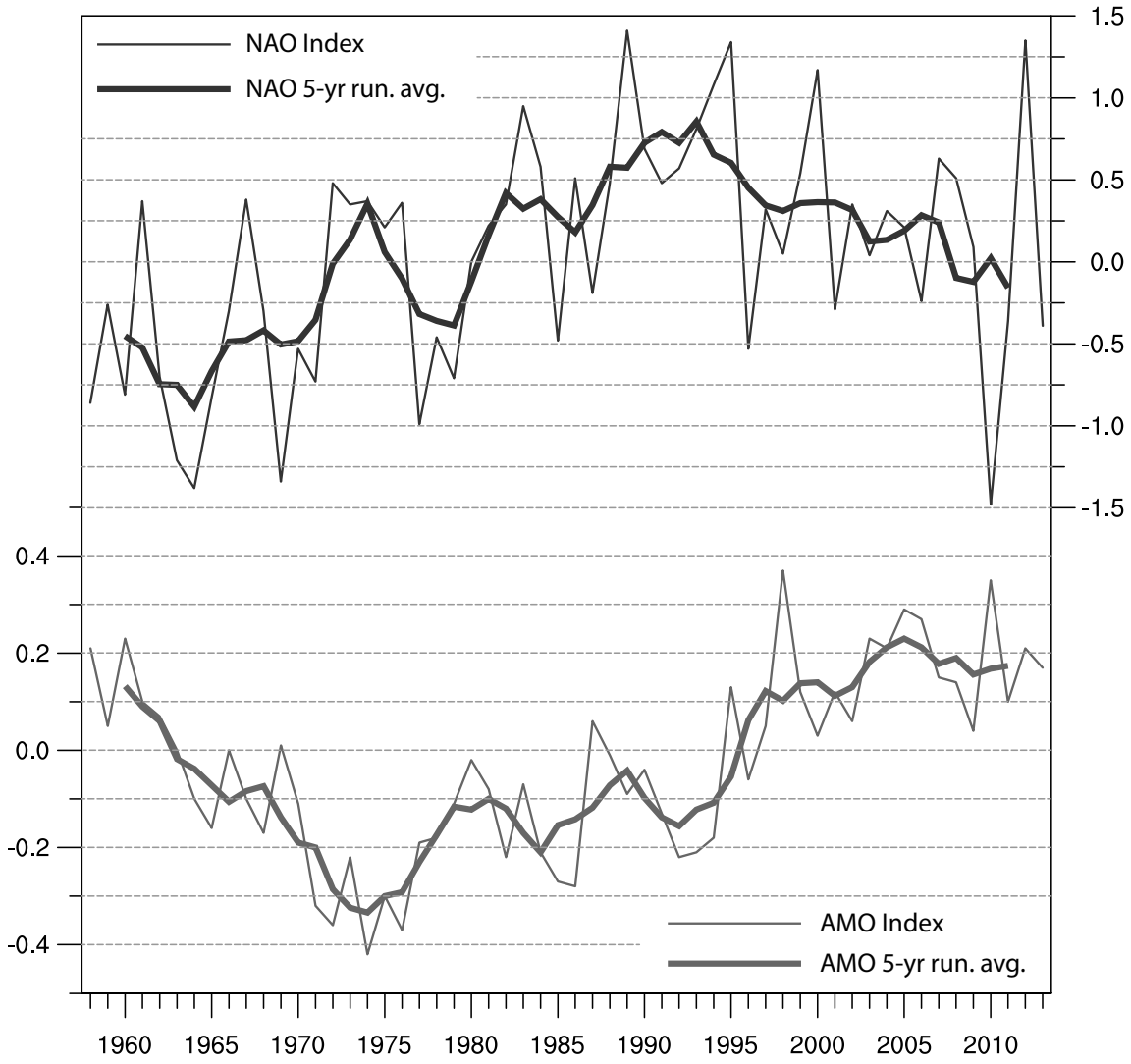

here are based on the 20th century average, rather than the 1964 – 1999 average as in Enfield et al. (2001), and not detrended, thus preserving the long-term warming trend. Linearly detrending the SST anomaly signal emphasizes the multidecadal characteristics, however removing the underlying warming trend caused by anthropogenic factors. The detrended AMO index is not suitable for this study because the recent anthropogenic forced warming is part of the South Greenland precipitation investigation. The AMO index used here not only shows the multidecadal fluctuations of North Atlantic SST over the last seven decades but also displays the overall increasing SST coinciding with the enhanced warming in the Arctic (Francis and Vavrus, 2012). This enhanced warming, or Arctic Amplification (as named in Francis and Vavrus, 2012), facilitates the weakening of the meridional thermal gradient leading to a decrease in westerly wind speeds. Weaker near surface westerlies, linked with Arctic Amplification, and the recent increase in greenhouse gases likely facilitate the warming of SSTs in the North Atlantic.

The JRA-55 reanalysis encompasses only one –AMO and one +AMO phase. The year 1963 marks the beginning of the recent AMO "cycle" resulting in a full -AMO phase (1964 – 1994) of anomalously cooler North Atlantic annual SSTs and the current +AMO phase (1996 – 2013) of anomalously warmer annual SSTs.

It should be noted that while these indices are useful to explain general circulation changes, since they combine several aspects of atmospheric states, indices do not explain the driving forces of synoptic weather. Furthermore, these indices are assumed to explain natural variability, however, these indices could be misinterpreted if warming due to anthropogenic forces influence the driving factors of the indices. In the case of the NAO, it is cyclone frequency (Rogers, 1990; and Serreze et al., 1997) and near surface

westerlies (Rogers 1985) that are the major drivers of T_{2m} and precipitation over the coastal regions of the North Atlantic domain, which in many cases correlate well with the NAO index. For the AMO, we favor the argument that SST is externally driven by the westerlies, as explained by Wunsch and Ferrari (2004). Thus, it is wind stress stimulating ocean surface mixing and SST, which influences T_{2m} and precipitation in many regions around the North Atlantic, which in many cases, again, correlates well with the AMO index.

3.2.5. Icelandic Low and Azores High

In our search for South Greenland precipitation drivers, we examine both of the pressure centers making up the NAO. The NAO index describes changes in the MSLP gradient between the Icelandic Low and Azores High and is often associated with the basic climatological variables T_{2m}, u_{10m}, v_{10m}, and precipitation. We first identify the locations of the seasonal and annual Icelandic Low and Azores High to show how both climatological pressure centers fluctuate and to correlate them to precipitation in South Greenland. There are two options, namely, the average of a stationary, or of a floating location. The conventional thought of the Icelandic Low location is in the Denmark Strait/Iceland region. However, the Icelandic Low is not stationary as it can be found in other locations, such as south of Greenland or farther north over the Greenland and Norwegian Seas. Here, we focus on the Icelandic Low in the most common location (proximal to Iceland) rather than the Icelandic Low changing location through time. Going with the first option is important for this investigation because of the counterclockwise flow around low pressures and these winds in the vicinity of South

Greenland. Thus, we discuss the Icelandic Low as defined as the average of monthly and yearly MSLP within 68°N – 58°N and 40°W – 20°W (Fig. 3.2) as per option 1.

The same approach is taken for defining the Azores High. Although the Azores High is generally more stationary when compared to the Icelandic Low, the general high pressure center locations fall over the Azores Islands or southwestern Europe (France and the Iberian Peninsula). Here, we define the Azores High as the monthly and yearly MSLP averaged over 40°N – 20°N and 40°W – 20°W (Fig. 3.2). We also show that, however rare, high pressure blocking patterns can persist over the northeast Atlantic, west of Portugal. These blocking patterns can be seen in a month average of the Azores High even though the Azores High is not an index for blocking patterns.

3.3. Results and Discussion

As discussed above, South Greenland is made up of two main climate regimes, the southwest and southeast. We will first discuss the evolution of precipitation in southwest Greenland and then the southeast followed by interannual variability of precipitation in both regions and how the Icelandic Low, Azores High, T_{2m}, 10-m winds, and blocking patterns influence precipitation across South Greenland.

The mean annual total precipitation over southwest Greenland (as shown by the gray box in Fig. 3.2) is 723 mm/year. Precipitation between 1964 – 1994 is generally lower than the mean, at an average of 693 mm/year, whereas after 1995, precipitation increases by about 9%, to an average of 753 mm/year (Fig. 3.2). The standard deviation of southwest Greenland precipitation also increases, by about 61%, from 66 to 106 ($p = 0.02$). The increase in precipitation and interannual variability corresponds to the shift

Figure 3.6 Surface temperature difference with respect to the AMO phase transition. Temperature at 2 m is temporally averaged over the previous -AMO phase (1964-1994) and subtracted from the current +AOM phase (1996-2013).

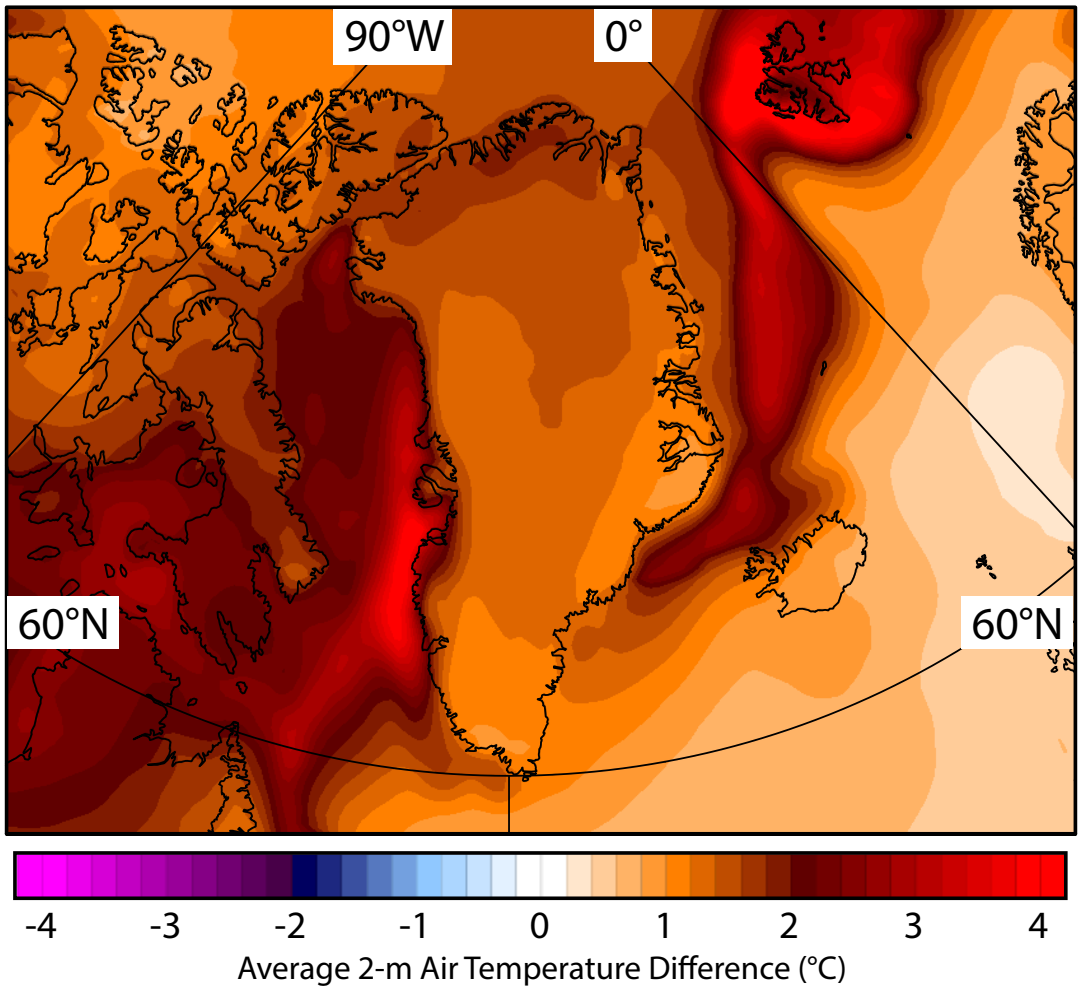

from the -AMO to +AMO phase in 1995 (Fig. 3.5). Additionally, this increase parallels to the general increase in T_{2m} over South Greenland (Fig. 3.6), which also corresponds to the 1995 AMO shift. Furthermore, the increase in SST since 1995 coincides with the recent enhanced warming of the Arctic, or Arctic Amplification (Francis and Vavrus 2012).

The mean annual total precipitation in southeast Greenland (as shown by the black box in Fig. 3.2) is 970 mm/year and shows a different pattern when compared to southwest Greenland precipitation. During the 1958 – 1983 period, southeast Greenland precipitation appears to be more variable than the 1984 – 2001 period with an apparent increase in variability following 2001. However, the described time periods fail the student t-test ($p >> 0.05$), suggesting that precipitation in southeast Greenland has not fluctuated on any long-term basis at least as produced by JRA-55.

The interannual extremes of both southwest and southeast Greenland precipitation coincide with the temporal changes of the strength of the Icelandic Low (Fig. 3.11) but are opposite in nature. One would therefore expect an anticorrelation between precipitation in southwest and southeast Greenland, but this is not the case ($r = 0.06$). To understand the Icelandic Low and its impacts on South Greenland precipitation, we discuss how the Icelandic Low is formed.

As low pressure systems traverse the North Atlantic from northeastern United States to Iceland, the Icelandic Low, an average of the low pressure centers over time, is found to be deep and situated proximal to Iceland (Rogers, 1990), as examples Feb 1984 and 1990 (Fig. 3.7). Inversely, as cyclones take a more variable path, the Icelandic Low is generally weaker and can be found south of Greenland. This can be explained by a

decrease in westerly wind speeds (Rogers, 1985), a decrease in frequency of low pressure systems (Rogers, 1990; and Serreze et al., 1997), and/or high pressure blocking patterns over the Northeast Atlantic (Barnston and Livezey, 1987; and Corte-Real et al., 1998). Examples of the latter are seen during the months of February 1983 and 2005 (Fig. 3.7).

South Greenland precipitation correlates to u_{10m} (Fig. 3.8, and Fig. 3.12 for seasonal correlations) on either side of the ridgeline, positively ($0.5 < r < 0.7$, $p < 0.5$) to the west and negatively ($-0.7 < r < -0.5$, $p < 0.5$) to the east, as expected, since orographic flow increases chances for precipitation. The easterlies which influence precipitation in southeast Greenland occur with cyclonic flow in the Denmark Strait (Fig. 3.9), thus seasons when the Icelandic Low is deep.

Precipitation chances are expected to increase in southwest Greenland when the Icelandic Low is weak, as seen by correlations of 0.5 – 0.7 ($p < 0.5$) between the Icelandic Low and precipitation (Fig. 3.11). This pattern is associated with increasing v_{10m} winds over southwest Greenland (correlations of 0.5 – 0.7, $p < 0.5$) between the Icelandic Low and v_{10m} (Fig. 3.9 and Fig. 3.13 for seasonal correlations). As the Icelandic Low is more pronounced in the winter months, and to a lesser extent the spring, the correlations decrease (0.4 – 0.6, $p < 0.5$) in southwest Greenland between the Icelandic Low and precipitation and v_{10m}.

Blocking patterns also play a role in where precipitation may fall over South Greenland. With persistent, high pressure blocking patterns over the northeast Atlantic, low pressure systems will take a poleward path around the high due to the outward, clockwise flow around the high. These blocking patterns can appear in the climatological Azores High. As discussed earlier, it should be noted that blocking patterns are rare and

Figure 3.7 Mean sea level pressure (left) and precipitation (right) averaged over February months of extreme precipitation and NAO phases. Positive NAO examples (a and b) with decrease in southwest Greenland precipitation (e and f). Negative NAO examples (c and d) with increase in southwest Greenland precipitation (g and h).

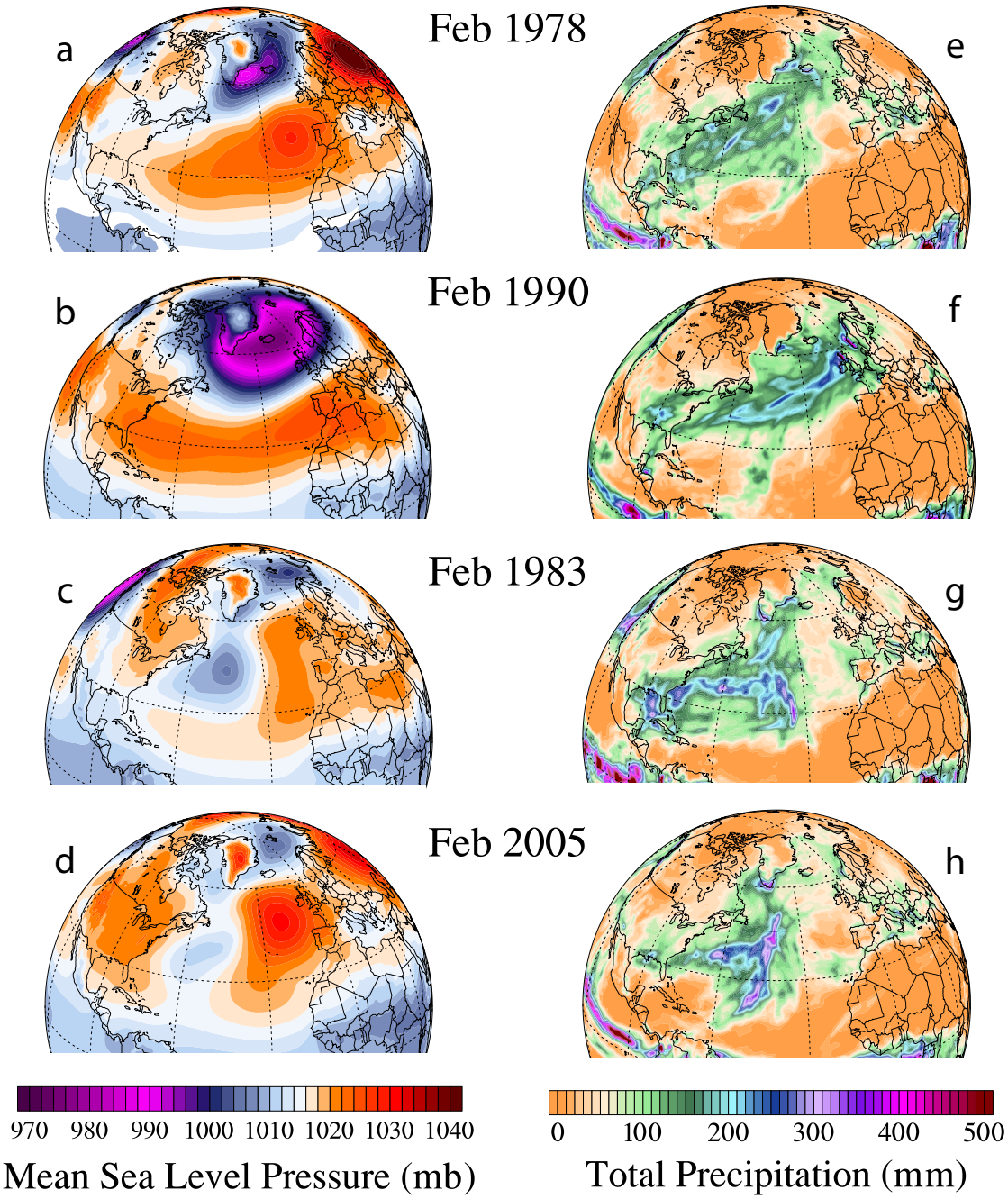

Figure 3.8 Annual correlation maps between precipitation and surface temperature (a), MSLP (b), 10-m u-winds (c), and 10-m v-winds (d).

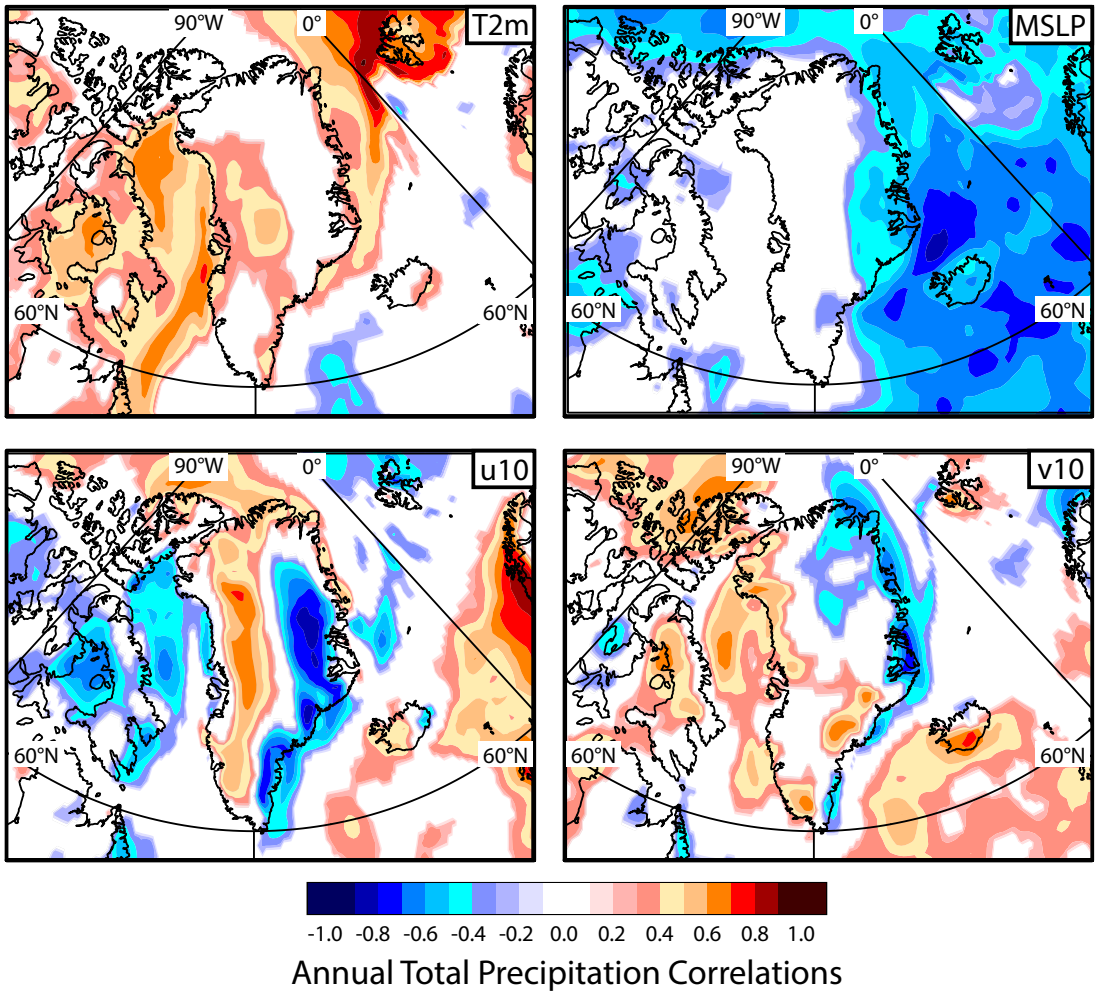

Figure 3.9 Annual correlation maps between the Icelandic Low and surface temperature (a), MSLP (b), 10-m u-winds (c), 10-m v-winds (d), and precipitation (e)

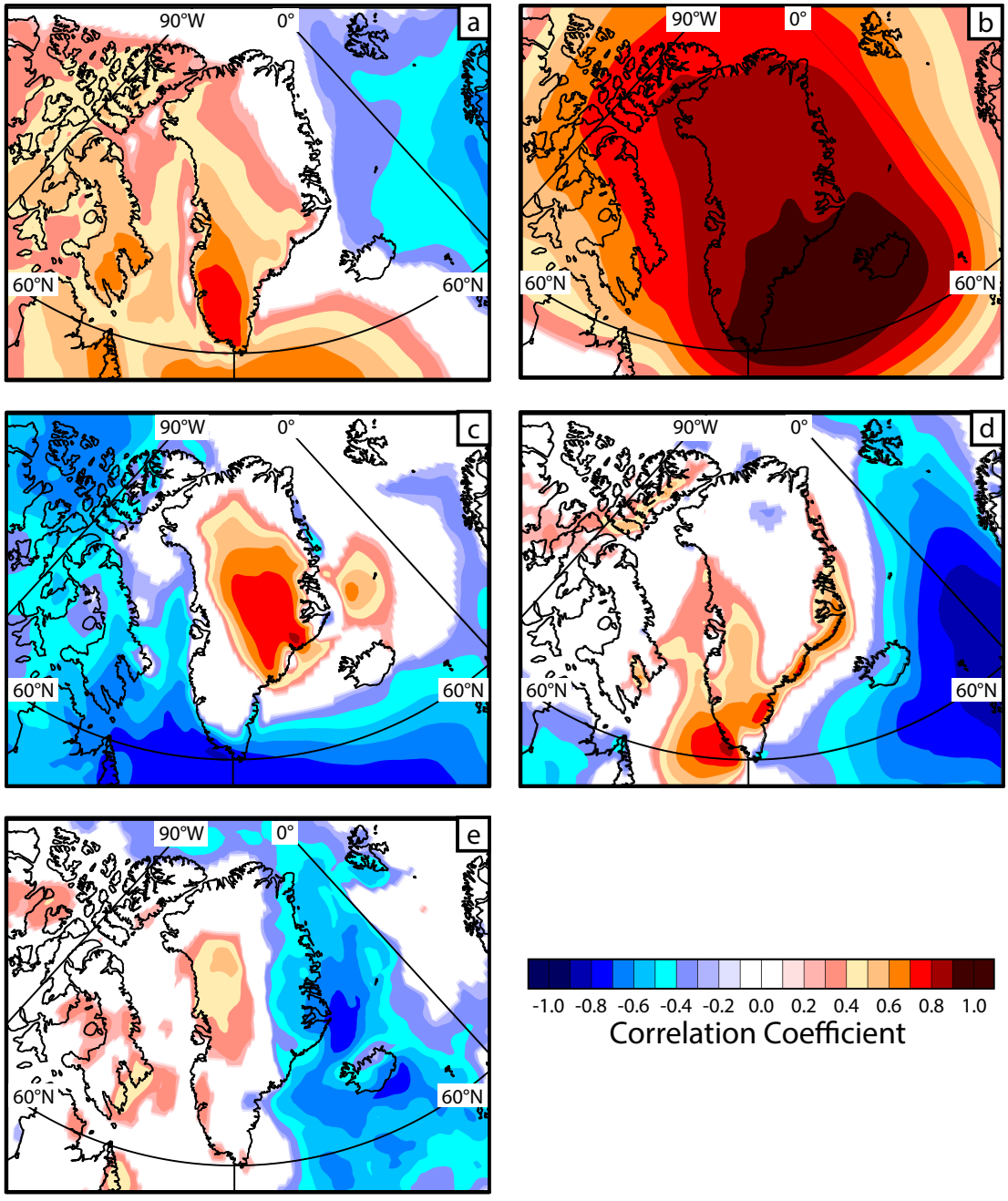

the Azores High is not an index for blocking patterns. We correlate the Azores High and find that the correlation is much lower ($-0.4 < r$ 0.0, $p < 0.5$) with precipitation, u_{10m}, and v_{10m} (Fig. 3.10) with respect to correlations made with the Icelandic Low. However, the anticorrelation ($-0.7 < r < -0.6$, $p < 0.5$) with T_{2m} in South Greenland suggests lower T_{2m} with a stronger Azores High (Fig. 3.9), opposite to that with the Icelandic Low. The correlations between the Azores High and precipitation in South Greenland (southwest: $r = -0.23$; southeast: $r = 0.29$) show that the Azores High plays a much smaller role in the interannual variability of South Greenland climate when compared to the Icelandic Low. Therefore, this result should suggest caution when using the NAO index to explain fluctuations of climate in South Greenland, as well as other regions.

During the two years of extreme precipitation, 1983 and 2005, February of both years (Fig. 3.7) show not only a weak Icelandic Low located south of Greenland but also a strong Azores High extending northward. This can be explained by the inclusion of a high pressure blocking pattern which persisted for upwards of two weeks during these February months, hence forcing cyclones to take a poleward path toward South Greenland. In these cases, southwest Greenland received more precipitation than other years with a decrease in the southeast. The existence of a blocking pattern influences cyclone tracks, thus increasing precipitation chances over Southwest Greenland. Francis and Vavrus (2012) suggest that these blocking patterns will increase as positive feedback systems, such as increased meridional transport weakening the zonal flow of the westerly winds, further enhance warming in the Arctic. Francis and Vavrus also discuss how long-amplitude ridging has increased in frequency since 2000 leading to an increase in

Figure 3.10 Annual correlation maps between the Azores High and surface temperature (a), MSLP (b), 10-m u-winds (c), 10-m v-winds (d), and precipitation (e)

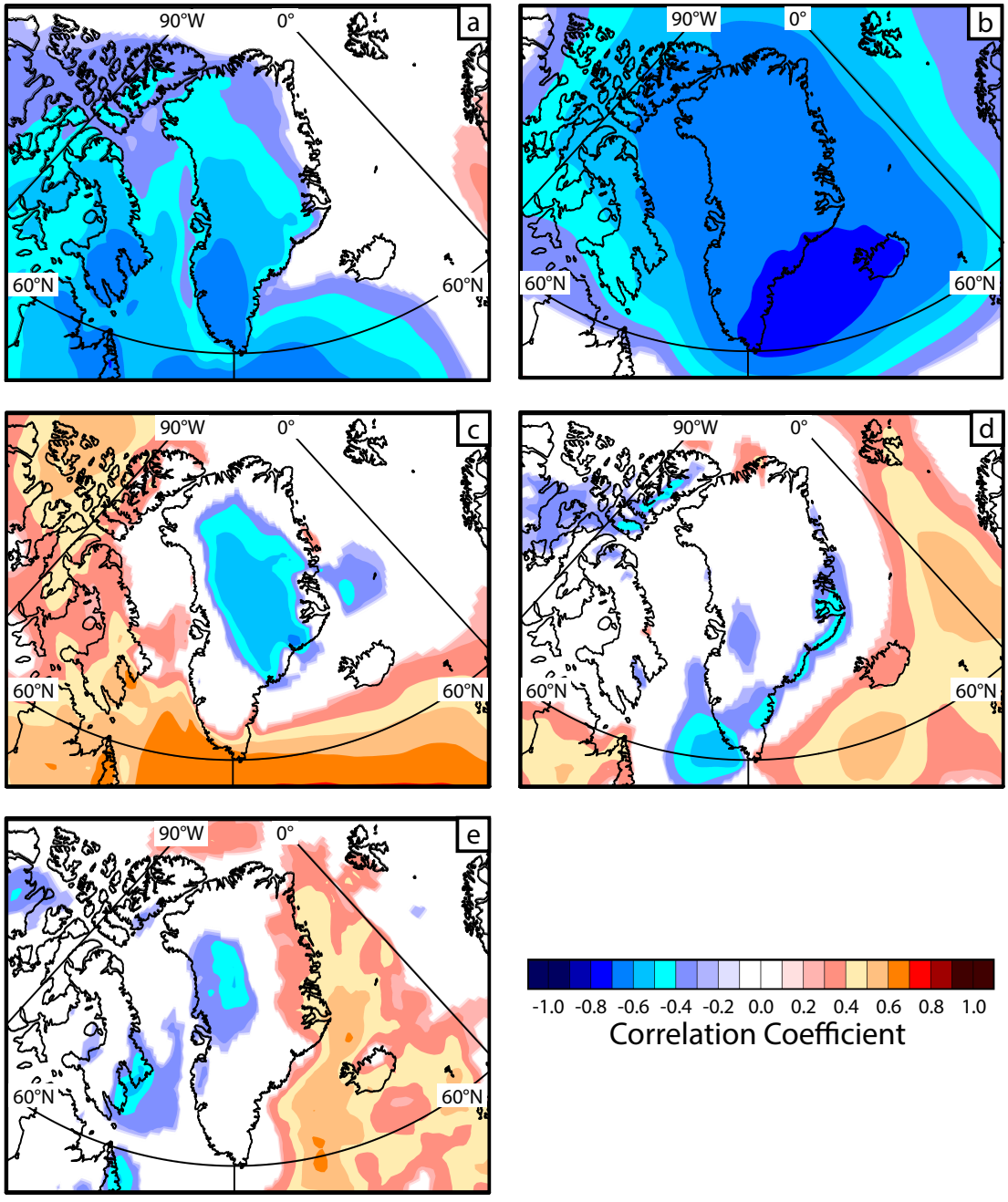

meridional flow, further facilitating Arctic Amplification due to the increase of meridional heat and moisture transport.

3.4. Conclusions

This work shows that precipitation, T_{2m}, and 10-m winds over South Greenland coincide most closely with the internal controllers of the NAO and AMO, and less so with the indices themselves. Both the NAO and AMO begin as a negative phase and end in a positive phase during the JRA-55 record, which coincides with the enhanced increase of Arctic temperatures and weakening of the meridional thermal gradient. As discussed earlier, an increase in meridional transport facilitates the increase in temperature at high latitudes leading to an increase in moisture availability. Not only are these circulation features a part of the positive feedback system associated with Arctic Amplification (Francis and Vavrus, 2012), but they also increase chances of precipitation in southwest Greenland over a long-term basis. As the zonal component of the westerlies decreases, due to a weakening meridional thermal gradient, the near surface wind field weakens, thus facilitating an increase in SST. The recent increase in North Atlantic SST is manifested in the positive mode of the AMO. Furthermore, as the meridional component of the wind field increases due to elongated, slow-moving ridges, precipitation and temperature across South Greenland will both increase, due to increased moisture and heat transport.

For years of extreme high and low precipitation (Fig. 3.7), February 1983 the Icelandic Low is located south of Greenland with a high pressure blocking pattern persisting just west of Europe for two weeks. In February 2005, the Icelandic Low is

almost nonexistent in association with another strong blocking pattern. As these blocking patterns develop, storms travel poleward west of the high pressure center and, in these cases, to southwest Greenland. In the absence of a blocking pattern, as seen in February of 1984 and 1990 (Fig. 3.7), cyclones take a predominantly northeastward path toward Iceland and Great Britain (Hurrell, 1995), instead bringing precipitation to southeast Greenland. The Icelandic Low being a feature throughout the year, although most prominent during winter months, the correlations with precipitation are strongest during the winter and decrease through the following seasons (Fig. 3.11).

In conclusion, precipitation across South Greenland is part of a complex system partially explained by the Icelandic Low, T_{2m}, u_{10m}, v_{10m}, MSLP, and blocking patterns. The strength of the Icelandic Low appears to be one of the major controllers of South Greenland precipitation (Fig. 3.9 and Fig. 3.11) operating in tandem with increasing T_{2m} (Fig. 3.6) and the near surface wind field (Figs. 3.13 and 3.14). As meridional and zonal wind components increase in the positive direction, the chances for precipitation over southwest Greenland increases, whereas zonal flow increasing in the negative direction (easterly), chances for precipitation in southeast Greenland increases. Southerly flow over the North Atlantic is often accompanied with an increase in temperature, thus increasing chances for precipitation across South Greenland. It should be expected that as the enhanced Arctic warming increases through time, elongated ridging, and blocking patterns, should become a less rare occurrence, further increasing precipitation over southwest Greenland, both in annual amount and variability, while decreasing the likelihood of precipitation over southeast Greenland.

Figure 3.11 Seasonal correlation maps between precipitation and the Icelandic Low for winter (DJF, a), spring (MAM, b), summer (JJA, c), and autumn (SON, d).

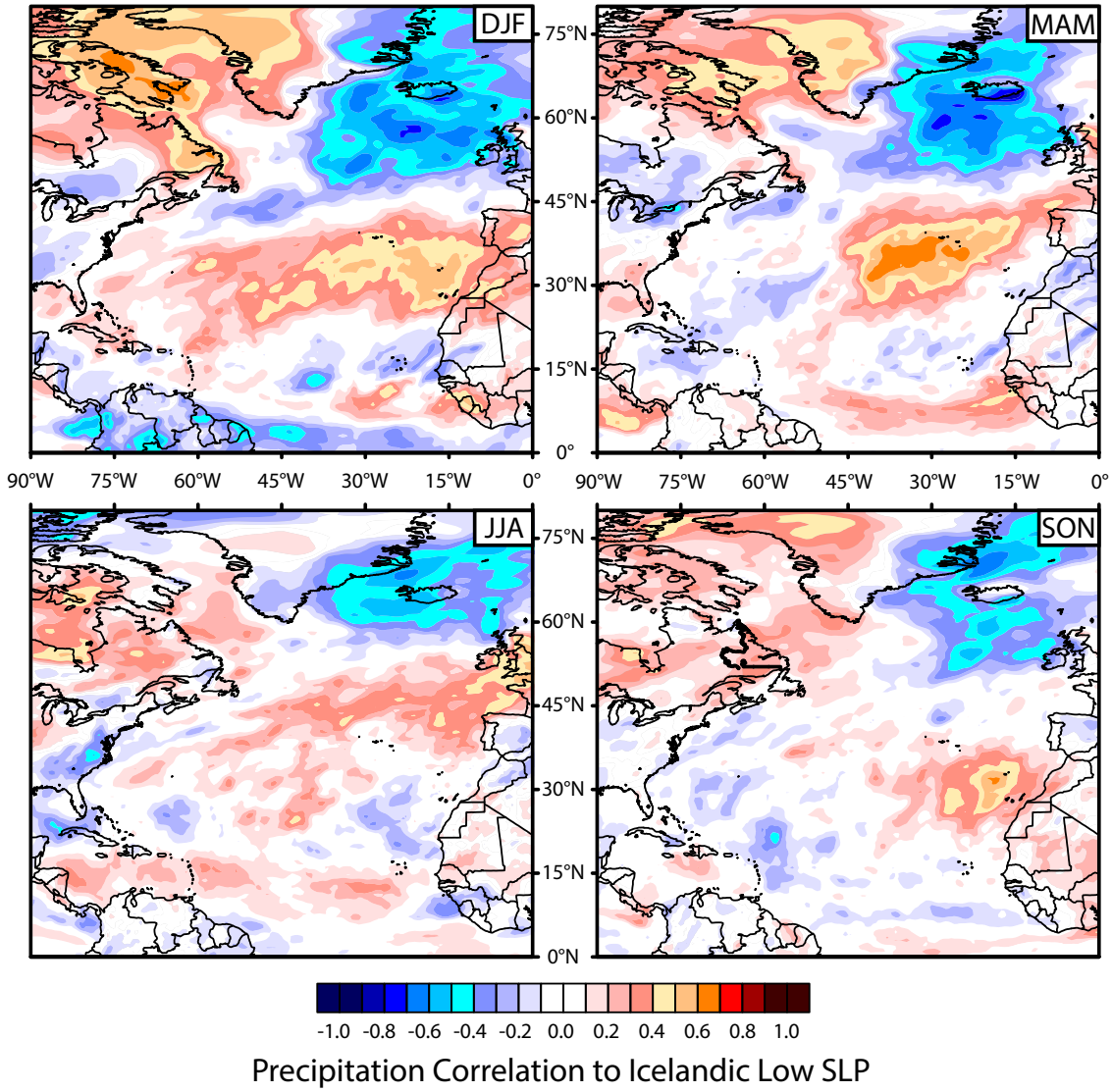

Figure 3.12 Seasonal correlation maps between precipitation and 10-m u-winds for winter (DJF, a), spring (MAM, b), summer (JJA, c), and autumn (SON, d).

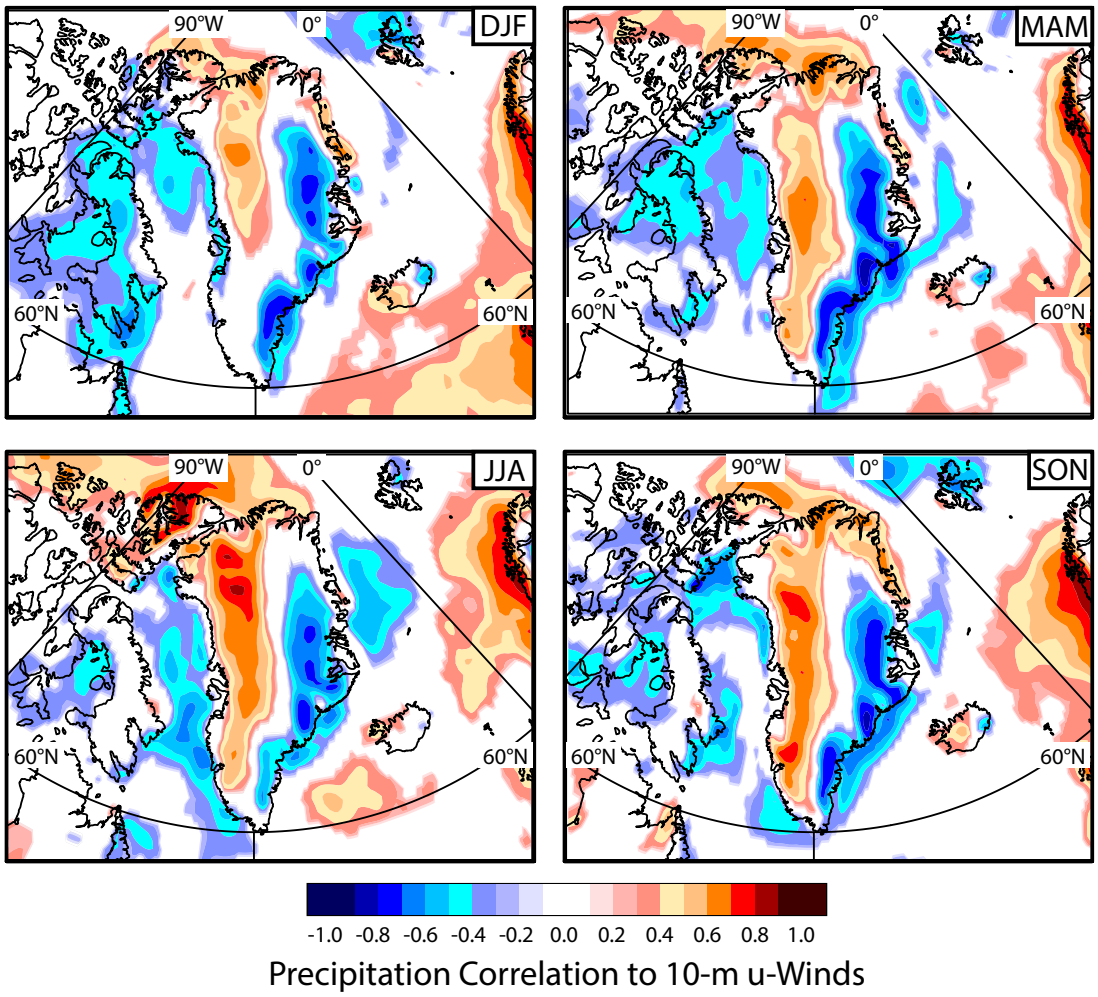

Figure 3.13 Seasonal correlation maps between 10-m v-winds and the Icelandic Low for winter (DJF, a), spring (MAM, b), summer (JJA, c), and autumn (SON, d).

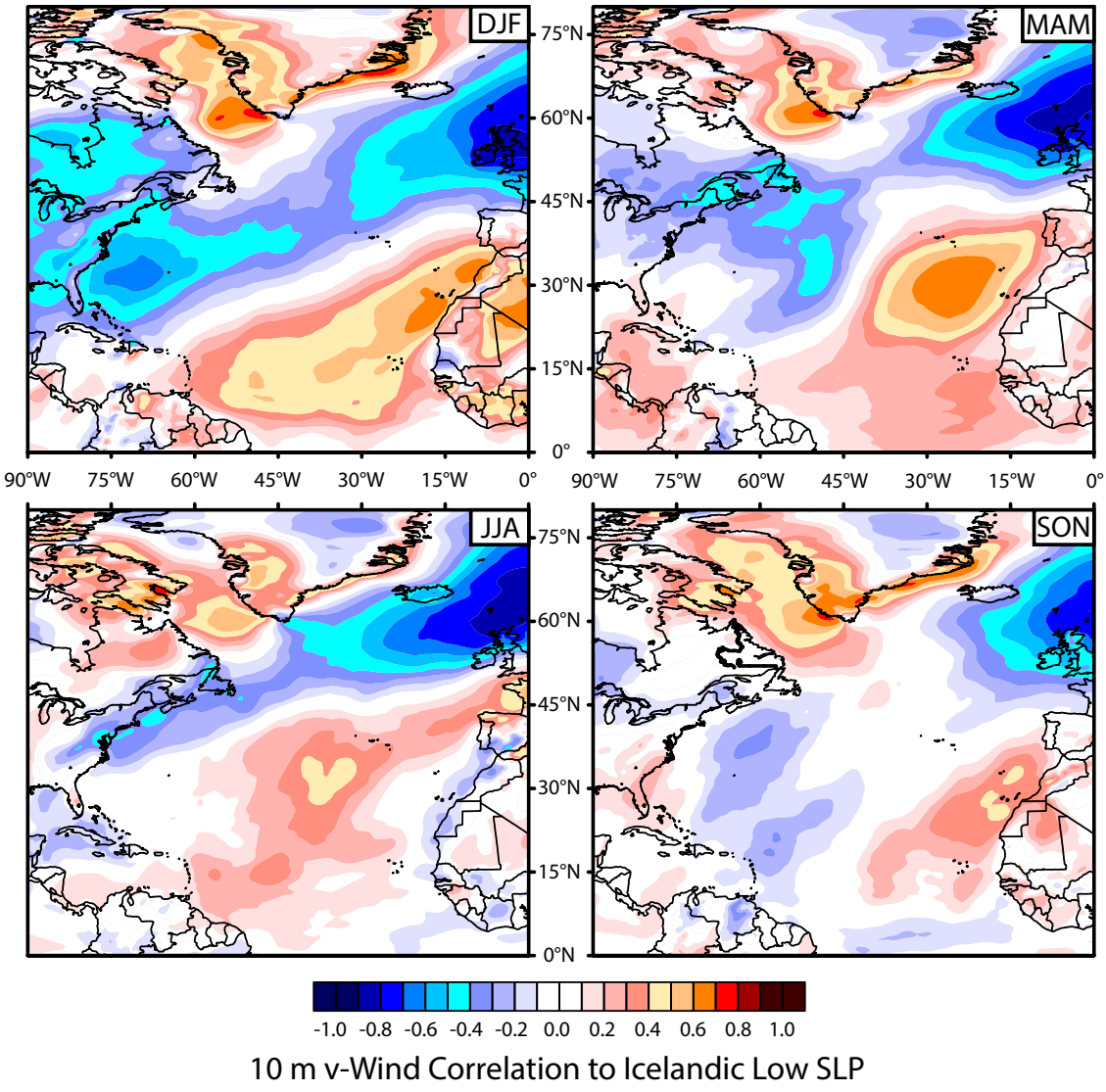

Figure 3.14 Seasonal correlation maps between precipitation and 10-m v-winds for winter (DJF, a), spring (MAM, b), summer (JJA, c), and autumn (SON, d).

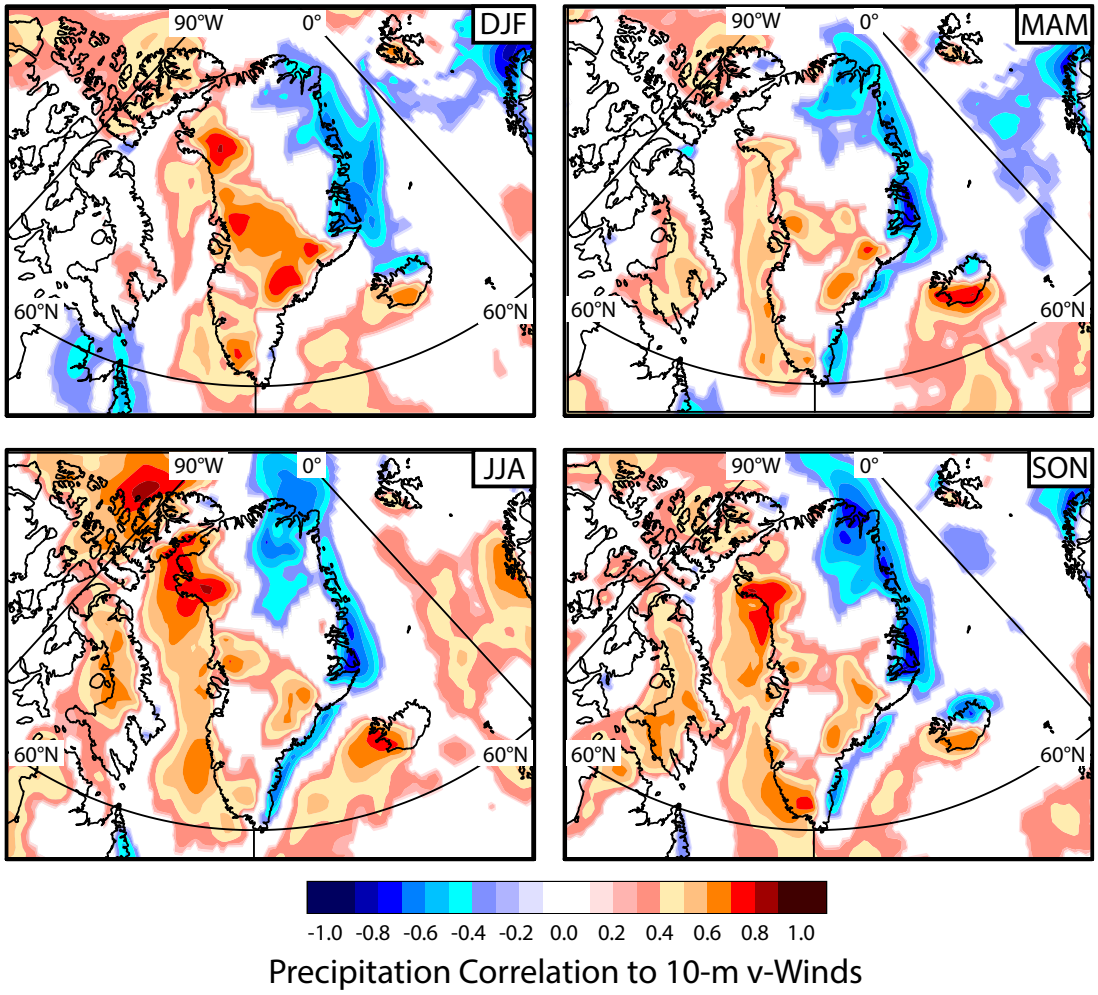

Figure 3.15 Seasonal correlation maps between precipitation and 2-m temperature for winter (DJF, a), spring (MAM, b), summer (JJA, c), and autumn (SON, d).

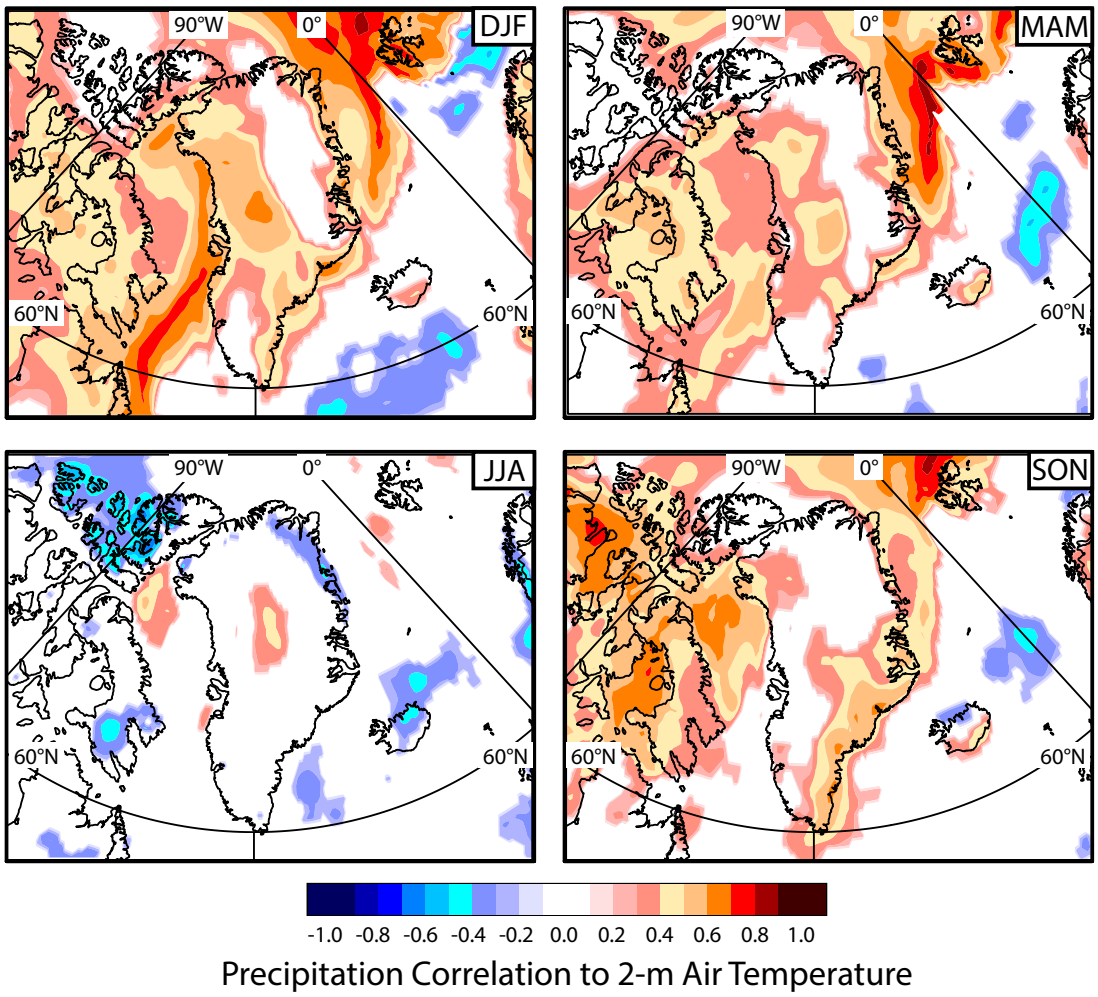

CHAPTER 4

CONCLUSIONS

This thesis presents an evaluation of an ensemble of four leading climate reanalysis models, and an investigation into the influences of atmospheric circulation over the North Atlantic on recent changes in precipitation over South Greenland. The latter study is derived from the GreenTrACS program connecting southwest Greenland precipitation to analyzed snow accumulation from snow and ice samples. Using these reanalyses in concert with meteorological observations it is possible to examine the influence of the North Atlantic Oscillation (NAO), Atlantic Multidecadal Oscillation (AMO), Icelandic Low, Azores High, blocking patterns, near surface westerly winds, and temperature on South Greenland precipitation.

Chapter 2 reports an examination of four leading global reanalysis models – CFSR, ERA-I, JRA-55, and MERRA – by comparing individual models against their ensemble average. Although all four reanalysis models are state-of-the-art, each exhibit differences resulting from internal physics and resolution that affects the spatial and temporal reproduction for targeted meteorological fields. For example, averaged global, land-based, 2-m air temperature (T_{2m}) from each reanalysis model has different annual temperatures, although, correlations between each reanalysis are high ($r > 0.88$) showing that each agree with the interannual patterns. The models are in agreement on large-scale precipitation for seasonal shifts in the Intertropical Convergence Zone (ITCZ), but differ on rainfall magnitude, and on rainfall pattern in the vicinity of islands and mountain ranges. In the free atmosphere, 500-mb geopotential heights (Z_{500}) differences between models are comparatively small, on the order of +/- 10 m. This favorable outcome likely

results because geostrophic flow is more easily simulated than flow within the friction layer.

Chapter 3 examines the influence of the North Atlantic Oscillation (NAO), Atlantic Multidecadal Oscillation (AMO), Icelandic Low, Azores High, blocking patterns, westerly winds, and temperature on precipitation across South Greenland. I find that statistically significant correlations are higher between precipitation and near surface winds and the Icelandic Low (of 0.5 – 0.7; $p < 0.5$) than correlations between precipitation and the NAO or AMO climate indices (southwest Greenland: $r = 0.12$ and 0.28, respectively; and southeast Greenland: $r = 0.25$ and -0.07, respectively). Moreover, recent warming coincides with both increased precipitation and increased interannual variability in southwest Greenland. I find that the precipitation signal in South Greenland is largely driven by the dynamics of middle latitude atmospheric circulation, most notably the Icelandic Low, the near surface westerly winds, and blocking patterns.

I suggest that the methods presented in this thesis be applied to daily and sub-daily time scales. Comparing daily and sub-daily precipitation and T_{2m} between third generation reanalyses will give insight on where the models diverge and how to improve the land surface schemes and data assimilation methods. Provided that there are small dissimilarities in the middle troposphere, finding sub-daily differences between reanalysis models would aid in finding how and where differences arise in the free atmosphere. The investigation of daily precipitation in South Greenland is also important to see how well reanalysis models, such as JRA-55, simulate large scale and convective storms in data-sparse regions. This is a non-trivial task, given that running a dynamical downscale model may be necessary for scale-relevant comparison of model results and point-based

meteorological observations. Nevertheless, further investigation into precipitation processes, moisture sources and transport, storm frequency, and microphysics is essential for better understanding the accuracy of simulated precipitation.

REFERENCES

Barnston, A. G., and R. E. Livezey, 1987: Classification, Seasonality and Persistence of Low-Frequency Atmospheric Circulation Patterns. *Mon. Wea. Rev.*, **115**, 1083-1126.

Bengtsson, L., S. Hagermann, and K. Hodges, 2004: Can climate trends be calculated from reanalysis data? *J. of Geophys. Res.*, **109**.

Birkel, S. D. and P. A. Mayewski, 2015: Analysis of Historical and Projected Future Climate of Mali, West African Sahel. Project Report. CGIAR Research Program on Climate Change, Agriculture, and Food Security. Copenhagen, Denmark. Available online at www.ccafs.cgiar.org.

Clement, A., K. Bellomo, L. N. Murphy, M. A. Cane, T. Mauritsen, G. Rädel, and B. Stevens, 2015: The Atlantic Multidecadal Oscillation without a role for ocean circulation. *Science*, **350**, 320-324.

Chen, G., T. Iwasaki, H. Qin, and W. Sha, 2014: Evaluation of the warm-season diurnal variability over East Asia in recent reanalysis JRA-55, ERA-Interim, NCEP CFSR, and NASA MERRA. *J. Climate*, **27**, 5517-5537.

Dee, D. P., and Coauthors, 2011: The ERA-Interim reanalysis: configuration and performance of the data assimilation system. *Quart. J. Roy. Meteor. Soc.*, **137**, 553-597.

de Leeuw, J., J. Methven, and M. Blackburn, 2015: Evaluation of ERA-Interim reanalysis precipitation products using England and Wales observations. *Quart. J. Roy. Meteor. Soc.*, **141**, 798-806.

Delworth, T. L. and M. E. Mann, 2000: Observed and simulated multidecadal variability in the Northern Hemisphere. *Clim. Dyn.*, **16**, 661-676.

Doyle, J. D., M. A. Shapiro, Q. Jiang, and D. L. Bartels, 2005: Large-Amplitude Mountain Wave Breaking over Greenland. *J. Atm. Sci.*, **62**, 3106-3126.

Enfield, D. B., A. M. Mestas-Nuñez, and P. J. Trimble, 2001: The Atlantic multidecadal oscillation and its relation to rainfall and river flows in the continental U.S. *Geophys. Res. Lett.*, **28**, 2077-2080.

Ensor, L. A. and S. M. Robeson, 2008: Statistical Charicteristics of Daily Precipitation: Comparisons of Gridded and Point Datasets. *J. App. Meteor. Clim.*, **47**, 2468-2476.

Francis, J. A., and S. J. Vavrus, 2012: Evidence linking Arctic amplification to extreme weather in mid-latitudes. *Geophys. Res. Let.*, **39**, L06801.

Gao, L., L. Hao, and X. Chen, 2014: Evaluation of ERA-Interim monthly temperature data over the Tibetan Plateau. *J. Mount. Sci.*, **11**, 1154-1168.

Hirahara, S., M Ishii, and Y. Fukuda, 2014: Centennial-Scale Sea Surface Temperature Analysis and Its Uncertainty. *J. Clim.*, **27**, 57-75.

Hurrell, J. W., 1995: Decadal Trends in the North Atlantic Oscillation: Regional Temperatures and Precipitation. *Science*, **269**, 676-679.

Hurrell, J. W., Y. Kushnir, G. Ottersen, M. Visbeck, 2003: The North Atlantic Oscillation: Climate Significance and Environmental Impact, Geophysical Monograph 134, American Geophysical Union.

Kalnay, E. and Coauthors, 1996: The NCEP/NCAR 40-Year Reanalysis Project. *Bull. Amer. Meteor. Soc.*, **77**, 437-471.

Kaplan, A., M. A. Cane, Y. Kushnir, A. C. Clement, M. B. Blumenthal, and B. Rajagopalan, Analyses of global sea surface temperature 1856-1991. *J. Geophys. Res.*, **103**, 18,567-18,589.

Kobayashi, S. and Coauthors, 2015: The JRA-55 Reanalysis: General specification and basic characteristics. *J. Meteorol. Soc. Jpn.*, **93**, 5-48.

Kumar, A., L. Zhang, and W. Wang 2014: Sea Surface Temperature-Precipitation Relationship in Different Reanalyses. *Mon. Wea. Rev.*, **141**, 1118-1123.

Lindsay, R., M. Wensnahan, A. Schweiger, and J. Zhang, 2014: Evaluation of seven different atmospheric reanalysis products in the Arctic. *J. Clim.*, **27**, 2588-2606.

Naud, C. M., J. F. Booth, and A. D. Del Genio, 2013: Evaluation of ERA-Interim and MERRA cloudiness in the Southern Ocean. *J. Clim.*, **27**, 2019-2124.

Ohmura, A., and N. Reeh, 1991: New precipitation and accumulation maps for Greenland, *J. Glaciol.*, **37**, 140-148.

Onogi, K., and Coauthors, 2007: The JRA-25 Reanalysis. *J. Meteorol. Soc. Jpn.*, **85**, 369-432.

Otterå, O. H., M. Bentsen, H. Drange, and L. Suo, 2010: External forcing as a metronome for multidecadal variability. *Nat. Geosci.*, **3**, 688-694.

Reynolds, R. W., T. M. Smith, C. Liu, D. B. Chelton, K. S. Casey, and M. G. Schlax, 2007: Daily High-Resolution-Blended Analysis for Sea Surface Temperature. *J. Clim.*, **20**, 5473-5496.

Rienecker, M. M., and Coauthors, 2011: MERRA: NASA's Modern-era retrospective analysis for research and applications. *J. of Clim.*, **24**, 3624-3648.

Rogers, J. C., 1985: Atmospheric Circulation Changes Associated with the Warming over the Northern North Atlantic in the 1920s. *J. Clim. Appl. Met.*, **24**, 1303-1310.

Rogers, J. C., 1990: Patterns of Low-Frequency Monthly Sea Level Pressure Variability (1899-1986) and Associated Wave Cyclone Frequencies. *J. Clim.*, **3**, 1364-1379.

Saha, S., and Coauthors, 2010: The NCEP climate forecast system reanalysis. *Bull. Amer. Meteor. Soc.*, **91**, 1015-1057.

Santer, B. D., and Coauthors, 2004: Identification of anthropogenic climate change using second-generation reanalysis. *J. Geophys. Res.*, **109**, D21104.

Schlesinger, M. E., and N. Ramankutty, 1994: An oscillation in the global climate system of period 65-70 years. *Nature*, **367**, 723-726.

Serreze, M. C., F. Carse, and R. G. Barry, 1997: Icelandic Low Cyclone Activity: Climatological Features, Linkages with the NAO, and Relationships with Recent Changes in the Northern Hemispheric Circulation. *J. Clim.*, **10**, 453-464.

Uppala, S. M., and Coauthors, 2005: The ERA-40 re-analysis. *Quart. J. Roy. Meteor. Soc.*, **131**, 2961-3012.

Walker, G. T., 1923: Correlation in seasonal variations of weather, VIII: A preliminary study of world weather. *Mem. Ind. Meteor. Dept.*, **24**, 275–332.

Walker, G. T. and E. W. Bliss, 1932: World weather. V. *Mem. Roy. Meteor. Soc.*, **103**, 29–64.

Wunsch, C., 1992: Decade-to-Century Changes in the Ocean Circulation. *Oceanography*, **5**, 99-106.

Wunsch, C., and R. Ferrari, 2004: Vertical Mixing, Energy, and the General Circulation of the Oceans. *Annu. Rev. Fluid Mech.*, **36**, 281-314.

Wunsch, C., 2006: Abrupt climate change: An alternative view. *Quat. Res.*, **65**, 191-203.

Yi, Y., J. Kimball, L. Jones, R. Reichle, and K. McDonald, 2011: Evaluation of MERRA land surface estimates in preparation of the soil moisture active passive mission. *J. Clim.*, **24**, 3797-3816.

Zhang, R. and T. L. Delworth, 2006: Impact of Atlantic multidecadal oscillations on India/Sahel rainfall and Atlantic hurricanes. *Geophys. Res. Lett.*, **33**, L17712.

APPENDIX

NCAR COMMAND LANGUAGE SCRIPTS

1. ensemble2netCDF.ncl

The following NCL script takes each of the four reanalysis model output for nine meteorological surface variables, averages each, and writes the averaged output as a netCDF file. This script was written largely from Dr. Sean D. Birkel's help.

```
1   load "$NCARG_ROOT/lib/ncarg/nclscripts/csm/contributed.ncl"
2   load "$NCARG_ROOT/lib/ncarg/nclscripts/esmf/ESMF_regridding.ncl"
3
4   ;================================================================
5   ; Write netCDF file
6   ;================================================================
7   procedure
8   write_nc(fprefix,outdir,outfile,gridres,ntime,nlat,nlon,time,\
9     lat,lon,T2,U10,V10,WS10,MSLP,SNOWD,TH2O,SEAICE,PRCP)
10
11  begin
12
13    ;Open output file
14    ;---------------------------------------------------------------
15    system("/bin/rm -f "+outdir+outfile)
16    fout=addfile(outdir+outfile,"c")
17    setfileoption(fout,"DefineMode",True)
18    print("Generating "+outdir+outfile)
19
20    ;Define global attributes
```

```
;---------------------------------------------------------------
fAtt=True
fAtt@title=fprefix+" Ensemble of 3rd Generation Reanalysis \
  Data Sets on "+gridres+"deg resolution"
fAtt@source_file="None"
fAtt@Conventions="None"
fAtt@creation_date=systemfunc("date")
fileattdef(fout,fAtt)

;Predefine coordinate variables and their dimensionality
;---------------------------------------------------------------
dimNames=(/"time","lat","lon"/)
dimSizes=(/ntime,nlat,nlon/)
dimUnlim=(/False,False,False/)
filedimdef(fout,dimNames,dimSizes,dimUnlim)

;Predefine dimensionality of variables to be written to file
;---------------------------------------------------------------
filevardef(fout,"time",typeof(time),getvardims(time))
filevardef(fout,"lat",typeof(lat),getvardims(lat))
filevardef(fout,"lon",typeof(lon),getvardims(lon))
filevardef(fout,"T2",typeof(T2),getvardims(T2))
filevardef(fout,"U10",typeof(U10),getvardims(U10))
filevardef(fout,"V10",typeof(V10),getvardims(V10))
filevardef(fout,"WS10",typeof(WS10),getvardims(WS10))
filevardef(fout,"MSLP",typeof(MSLP),getvardims(MSLP))
filevardef(fout,"SNOWD",typeof(SNOWD),getvardims(SNOWD))
filevardef(fout,"TH2O",typeof(TH2O),getvardims(TH2O))
filevardef(fout,"SEAICE",typeof(SEAICE),getvardims(SEAICE))
```

```
50      filevardef(fout,"PRCP",typeof(PRCP),getvardims(PRCP))
51
52      ;Copy variable attributes to file
53      ;-----------------------------------------------------------------
54      filevarattdef(fout,"time",time)
55      filevarattdef(fout,"lat",lat)
56      filevarattdef(fout,"lon",lon)
57      filevarattdef(fout,"T2",T2)
58      filevarattdef(fout,"U10",U10)
59      filevarattdef(fout,"V10",V10)
60      filevarattdef(fout,"WS10",WS10)
61      filevarattdef(fout,"MSLP",MSLP)
62      filevarattdef(fout,"SNOWD",SNOWD)
63      filevarattdef(fout,"TH2O",TH2O)
64      filevarattdef(fout,"SEAICE",SEAICE)
65      filevarattdef(fout,"PRCP",PRCP)
66
67      setfileoption(fout,"DefineMode",False)
68
69      fout->time=(/time/)
70      fout->lat=(/lat/)
71      fout->lon=(/lon/)
72      fout->T2=(/T2/)
73      fout->U10=(/U10/)
74      fout->V10=(/V10/)
75      fout->WS10=(/WS10/)
76      fout->MSLP=(/MSLP/)
77      fout->SNOWD=(/SNOWD/)
78      fout->TH2O=(/TH2O/)
```

```
  fout->SEAICE=(/SEAICE/)
  fout->PRCP=(/PRCP/)
end

;================================================================
; Main Program
;================================================================
begin

  outdir="./"
  indir="./"
  do YYYY=2011,2013
    print(YYYY+"")
    gridres="0.5"
    fprefix="GEN3ENS"

    CFSR=addfile(indir+"CFSR/CFSR_sfc_"+YYYY+"_monthly.nc","r")
    ERAI=addfile(indir+"ERAI/ERAI_sfc_"+YYYY+"_monthly.nc","r")
    JRA=addfile(indir+"JRA/JRA_sfc_"+YYYY+"_monthly.nc","r")
    MERRA=addfile(indir+"MERRA/MERRA_sfc_"+YYYY+"_monthly.nc",\
      "r")

    outfile=fprefix+"_sfc_"+YYYY+"_monthly.nc"

    nlat=361
    nlon=720
    gridres_deg="0.5x0.5"
    lat=fspan(-90,90,nlat)
    llon=ispan(0,nlon,1)
```

```
lon=tofloat(llon(0:nlon-1))*.5
lon=decimalPlaces(lon,1,True)

time=new((/17/),"integer")
time!0="time"
time@long_name="Time"
time@units="months"
time@_FillValue=-9999
time@_CoordinateAxisType="Month"
time=ispan(1,17,1)
ntime=dimsizes(time)

lat!0="lat"
lat@long_name="latitude"
lat@grid_type="Latitude/Longitude"
lat@_CoordinateAxisType="Lat"
lat@units="degrees_north"

lon!0="lon"
lon@long_name="longitude"
lon@grid_type="Latitude/Longitude"
lon@_CoordinateAxisType="Lon"
lon@units="degrees_east"

T2=new((/ntime,nlat,nlon/),"float")
T2!0="time"
T2!1="lat"
T2!2="lon"
T2&time=time
```

```
T2&lat=lat
T2&lon=lon

U10=new((/ntime,nlat,nlon/),"float")
U10!0="time"
U10!1="lat"
U10!2="lon"
U10&time=time
U10&lat=lat
U10&lon=lon

V10=new((/ntime,nlat,nlon/),"float")
V10!0="time"
V10!1="lat"
V10!2="lon"
V10&time=time
V10&lat=lat
V10&lon=lon

WS10=new((/ntime,nlat,nlon/),"float")
WS10!0="time"
WS10!1="lat"
WS10!2="lon"
WS10&time=time
WS10&lat=lat
WS10&lon=lon

MSLP=new((/ntime,nlat,nlon/),"float")
MSLP!0="time"
```

```
166       MSLP!1="lat"
167       MSLP!2="lon"
168       MSLP&time=time
169       MSLP&lat=lat
170       MSLP&lon=lon
171
172       SNOWD=new((/ntime,nlat,nlon/),"float")
173       SNOWD!0="time"
174       SNOWD!1="lat"
175       SNOWD!2="lon"
176       SNOWD&time=time
177       SNOWD&lat=lat
178       SNOWD&lon=lon
179
180       TH2O=new((/ntime,nlat,nlon/),"float")
181       TH2O!0="time"
182       TH2O!1="lat"
183       TH2O!2="lon"
184       TH2O&time=time
185       TH2O&lat=lat
186       TH2O&lon=lon
187
188       SEAICE=new((/ntime,nlat,nlon/),"float")
189       SEAICE!0="time"
190       SEAICE!1="lat"
191       SEAICE!2="lon"
192       SEAICE&time=time
193       SEAICE&lat=lat
194       SEAICE&lon=lon
```

```
195
196       PRCP=new((/ntime,nlat,nlon/),"float")
197       PRCP!0="time"
198       PRCP!1="lat"
199       PRCP!2="lon"
200       PRCP&time=time
201       PRCP&lat=lat
202       PRCP&lon=lon
203
204       do m=0,16
205         print("m="+m)
206
207         T2_CFSR=CFSR->T2(m,:,:)
208         T2_ERAI=ERAI->T2(m,:,:)
209         T2_JRA=JRA->T2(m,:,:)
210         T2_MERRA=MERRA->T2(m,:,:)
211         T2(m,:,:)=(T2_CFSR+T2_ERAI+T2_JRA+T2_MERRA)/4
212
213         U10_CFSR=CFSR->U10(m,:,:)
214         U10_ERAI=ERAI->U10(m,:,:)
215         U10_JRA=JRA->U10(m,:,:)
216         U10_MERRA=MERRA->U10(m,:,:)
217         U10(m,:,:)=(U10_CFSR+U10_ERAI+U10_JRA+U10_MERRA)/4
218
219         V10_CFSR=CFSR->V10(m,:,:)
220         V10_ERAI=ERAI->V10(m,:,:)
221         V10_JRA=JRA->V10(m,:,:)
222         V10_MERRA=MERRA->V10(m,:,:)
223         V10(m,:,:)=(V10_CFSR+V10_ERAI+V10_JRA+V10_MERRA)/4
```

```
224
225         WS10_CFSR=CFSR->WS10(m,:,:)
226         WS10_ERAI=ERAI->WS10(m,:,:)
227         WS10_JRA=JRA->WS10(m,:,:)
228         WS10_MERRA=MERRA->WS10(m,:,:)
229         WS10(m,:,:)=(WS10_CFSR+WS10_ERAI+WS10_JRA+WS10_MERRA)/4
230
231         MSLP_CFSR=CFSR->MSLP(m,:,:)
232         MSLP_ERAI=ERAI->MSLP(m,:,:)
233         MSLP_JRA=JRA->MSLP(m,:,:)
234         MSLP_MERRA=MERRA->MSLP(m,:,:)
235         MSLP(m,:,:)=(MSLP_CFSR+MSLP_ERAI+MSLP_JRA+MSLP_MERRA)/4
236
237         SNOWD_CFSR=CFSR->SNOWD(m,:,:)
238         SNOWD_ERAI=ERAI->SNOWD(m,:,:)
239         SNOWD_JRA=JRA->SNOWD(m,:,:)
240         SNOWD_MERRA=MERRA->SNOWD(m,:,:)
241         SNOWD(m,:,:)=(SNOWD_CFSR+SNOWD_ERAI+SNOWD_JRA+\
242           SNOWD_MERRA)/4
243
244         TH2O_CFSR=CFSR->TH2O(m,:,:)
245         TH2O_ERAI=ERAI->TH2O(m,:,:)
246         TH2O_JRA=JRA->TH2O(m,:,:)
247         TH2O_MERRA=MERRA->TH2O(m,:,:)
248         TH2O(m,:,:)=(TH2O_CFSR+TH2O_ERAI+TH2O_JRA+TH2O_MERRA)/4
249
250         SEAICE_CFSR=CFSR->SEAICE(m,:,:)
251         SEAICE_ERAI=ERAI->SEAICE(m,:,:)
252         SEAICE_JRA=JRA->SEAICE(m,:,:)
```

```
253         SEAICE_MERRA=MERRA->SEAICE(m,:,:)
254         SEAICE(m,:,:)=(SEAICE_CFSR+SEAICE_ERAI+SEAICE_JRA+\
255           SEAICE_MERRA)/4
256
257         PRCP_CFSR=CFSR->PRCP(m,:,:)
258         PRCP_ERAI=ERAI->PRCP(m,:,:)
259         PRCP_JRA=JRA->PRCP(m,:,:)
260         PRCP_MERRA=MERRA->PRCP(m,:,:)
261         PRCP(m,:,:)=(PRCP_CFSR+PRCP_ERAI+PRCP_JRA+PRCP_MERRA)/4
262       end do
263     write_nc(fprefix,outdir,outfile,gridres,ntime,nlat,nlon,time,\
264       lat,lon,T2,U10,V10,WS10,MSLP,SNOWD,TH2O,SEAICE,PRCP)
265     end do
266   end
```

BIOGRAPHY OF THE AUTHOR

Jeffrey Daniel Auger was born in Portsmouth, NH to David Auger and Laurie Vezina in August 1983. He attended Metropolitan State University of Denver and graduated with two Bachelor of Science degrees in Meteorology and Applied Mathematics. During this time, he took on two internships in the Denver Metropolitan area: 1) Urban Drainage and Flood Control District (UDFCD), and 2) University Corporation for Atmospheric Research (UCAR). At both UDFCD and UCAR, he had the opportunity to better understand and forecast liquid and frozen precipitation in the Front Range of Colorado.

Jeffrey graduated MSU Denver in May 2013 and moved back to Maine that August to pursue a Master of Science degree at the University of Maine under the advisement of Drs. Kirk A. Maasch and Paul A. Mayewski. He was then awarded a research assistant position under Dr. Sean D. Birkel in September 2014. At the University of Maine, he focused on global climate reanalysis models and North Atlantic climate processes. Jeffrey is a candidate for the Master of Science degree in Quaternary and Climate Studies from the University of Maine in December 2016.